

### Key Points:

- Deeply penetrating thrust faults form along the crust–mantle interface beneath numerous lunar mascon basins, comprising (partial) ring fault systems
- Shortening strain is localized along the crust–mantle boundary by the subsidence of a superisostatic mantle plug and uplift of a thickened crustal collar
- In places, the formation of this (partial) ring-fault system was likely impeded by a combination of basin formation timing and prevailing heat flux

### Supporting Information:

Supporting Information may be found in the online version of this article.

### Correspondence to:

P. K. Byrne,  
[paul.byrne@wustl.edu](mailto:paul.byrne@wustl.edu)

### Citation:

Collins, M. S., Byrne, P. K., Klimczak, C., & Mazarico, E. (2023). Thrust faults bound an elevated mantle plug beneath several lunar basins. *Journal of Geophysical Research: Planets*, 128, e2022JE007682. <https://doi.org/10.1029/2022JE007682>

Received 15 NOV 2022

Accepted 6 DEC 2022

### Author Contributions:

**Conceptualization:** Paul K. Byrne, Christian Klimczak

**Formal analysis:** Matthew S. Collins, Paul K. Byrne

**Funding acquisition:** Paul K. Byrne, Christian Klimczak, Erwan Mazarico

**Investigation:** Matthew S. Collins, Paul K. Byrne

**Methodology:** Matthew S. Collins, Paul K. Byrne

**Project Administration:** Paul K. Byrne

**Resources:** Erwan Mazarico

**Supervision:** Paul K. Byrne

**Validation:** Christian Klimczak, Erwan Mazarico

**Writing – original draft:** Matthew S. Collins, Paul K. Byrne

## Thrust Faults Bound an Elevated Mantle Plug Beneath Several Lunar Basins

Matthew S. Collins<sup>1</sup> , Paul K. Byrne<sup>2</sup> , Christian Klimczak<sup>3</sup> , and Erwan Mazarico<sup>4</sup> 

<sup>1</sup>Department of Geosciences, University of Massachusetts Amherst, Amherst, MA, USA, <sup>2</sup>Department of Earth and Planetary Sciences, Washington University in St. Louis, St. Louis, MO, USA, <sup>3</sup>Department of Geology, University of Georgia, Athens, GA, USA, <sup>4</sup>NASA Goddard Space Flight Center, Greenbelt, MD, USA

**Abstract** The lunar maria are large expanses of basalt that infill antecedent impact basins and show evidence for postplacement deformation. Landforms within many of these basins suggest a period of compressive tectonics, although their formation mechanism has yet to be established. Previous work for Mare Crisium demonstrated that basin-circumferential wrinkle ridges, which typically demarcate the inner edge of an annulus of elevated terrain, are the result of deep-seated thrust faults that preferentially form along the boundary of an elevated superisostatic portion of mantle and a thick, subsostatic collar of crustal material. Here, we show that a similar fault architecture exists for several other mascon-bearing basins, including Maria Serenitatis, Nectaris, Moscovia, and, to a lesser degree, Humorum and Imbrium. These deeply penetrating basin-circumferential thrust faults, as for Mare Crisium, form a (partial) outward-dipping ring-fault system that bounds the elevated mantle plug beneath each basin as a geometric consequence of mascon evolution. If this geometric arrangement is unique to the Moon, then some characteristic(s) of lunar mascon evolution enables the formation of such mascon-bounding faults. Despite the ubiquitous nature of mascon-bound thrust ring faults at several lunar basins, whether such structures exist at mascon basins on other terrestrial worlds remains an open question.

**Plain Language Summary** The history of the Moon is violent and characterized by giant impacts, the largest of which are expressed as vast depressions that were later filled with basaltic lavas. The topography within these impact basins suggests that they have been tectonically deformed, with the source of this tectonic deformation long subject to debate. In this study, we examine several large impact basins that host a concentration of mass, or a “mascon,” under the ground. This mascon can be observed with the lunar gravity field data and is a result of the impact event itself. Features attributed to compressive stresses called “wrinkle ridges” are typically found in a circular pattern around the boundary of this mascon. We show that these structures sit on top of thrust faults that extend several tens of kilometers into the Moon’s interior and outline the mascon in three dimensions. We have discovered these deep faults in several basins on the lunar near- and far sides, including Mare Crisium, Serenitatis, Nectaris, Moscovia, Humorum, and Imbrium. It remains to be seen whether this property of lunar mascon basins is also present on other rocky worlds such as Mercury and Mars.

## 1. Introduction

The lunar mare basins host vast deposits of tholeiitic basalt, which is compositionally comparable to mid-ocean ridge basalts on Earth (Wedepohl, 1981). Formed early in Solar System history (possibly between ~4.2 and 3.8 Ga; Fassett et al., 2012; Stöffler et al., 2006), many of the Moon’s large impact basins were subsequently infilled by periodic, effusive volcanism over the subsequent 2.7 Gyr (Hiesinger et al., 2000, 2010, 2011). These mare-hosting basins show evidence for postplacement deformation by tectonic processes (Bryan, 1973; Maxwell et al., 1975; Solomon & Head, 1980), suggesting that the tectonic activity lasted well beyond the period of initial basin formation. However, the process(es) acting to deform these ponded basalt deposits, and the stresses driving that deformation, have not yet been fully characterized.

### 1.1. Formation of Mascon Basins and Subsequent Deformation

Lunar maria are characterized by a relatively low spectral reflectance and spatial crater density. Free-air gravity anomaly signatures for several such basins resemble a bulls-eye pattern (Zuber et al., 2013), with a broad central positive anomaly peak surrounded by an annulus of negative values and another ring of positive values farther out

**Writing – review & editing:** Matthew S. Collins, Paul K. Byrne, Christian Klimczak, Erwan Mazarico

again (Melosh et al., 2013). The central positive Bouguer gravity anomaly is thought to be indicative of superisostatic mantle material (a “mantle plug”: Neumann et al., 1996) and is termed as “mascon” (i.e., a mass concentration) (Muller & Sjogren, 1968). Under this interpretation, the superisostatic state of the mantle is a result of the mechanical coupling of the melt sheet and uppermost mantle with a subisostatic crustal collar immediately after impact (Melosh et al., 2013). As this crustal collar slowly uplifted toward isostatic equilibrium, the coupled mantle material achieved and maintained a superisostatic state (Freed et al., 2014).

These basins also show signs of considerable tectonic deformation (Bryan, 1973), which has been attributed to the subsidence of volcanic deposits (Maxwell et al., 1975) that likely occurred throughout mare emplacement (Solomon & Head, 1980). Shortening strain is manifested as structures termed “wrinkle ridges,” which are interpreted as folds over blind or surface-breaking thrust faults (e.g., Golombek, 1985; Golombek et al., 1991; Schultz, 2000). Wrinkle ridges are often concentrated along the inner perimeter of the mare basins, although many individual ridges occur throughout the mare. The exact geometry of the faults responsible for generating these landforms on the Moon and elsewhere has, historically, been the subject of debate as to whether they are thin- or thick-skinned tectonic structures (e.g., Byrne et al., 2015; Golombek et al., 2001; Mangold et al., 1998; Montési & Zuber, 2003; Watters, 1991; Zuber, 1995).

Mare Crisium, situated within the inner ring of a Nectarian-aged basin (Fassett et al., 2012; Stöffler et al., 2006) on the lunar near side (Figure 1), hosts a circumferential set of wrinkle ridges demarcating the inner edge of an annulus of elevated topography, or topographic bench (Byrne et al., 2015; Zisk et al., 1978). The relief across these landforms is as much as 500 m in places; wrinkle ridges occur along nearly the entire inner perimeter. Notably, these concentric ridges delineate the boundary of the peak-positive Bouguer gravity anomaly within the basin (Byrne et al., 2015).

## 1.2. Formation of Shortening Structures Within Mare Crisium

Earlier work for Mare Crisium (Byrne et al., 2015) serves as the motivation for this investigation, in which we search for and model similar landforms within several other mare basins. Finite-element modeling by Byrne et al. (2015) demonstrated that the subsidence of a superisostatic mantle plug, coupled with the uplift of a subisostatic crustal collar, will concentrate stresses in such a way as to induce slip along outward-dipping thrust faults within the basin that are subparallel to the crust–mantle interface at depth. Byrne et al. (2015) showed that a network of outward-dipping thrust faults accommodates upward of 1,000 m of displacement. These faults started forming immediately after the basin-forming impact and together comprise a ring-fault system that penetrates some 20 km into the lunar lithosphere and geometrically bounds the superisostatic mantle plug (Byrne et al., 2015). To deform the mare infill, however, deformation must have continued throughout the emplacement of mare basalts. The timing of the most recent deformation is as yet unknown but by definition postdates the last major volcanic infill episode.

A similar topographic signature is observed for the Orientale basin, although this signature has been attributed to thermal contraction of the postimpact melt pool (Vaughan et al., 2013; Wilson & Head, 2011). In Mare Crisium, at least, the architecture of the faults underlying the concentric shortening structures suggests that crustal shortening along the perimeter of the basin also reflects the isostatic adjustment of the mantle plug and crustal collar, as opposed to solely the cooling and subsidence of the mare basalts. We expand on the work by Byrne et al. (2015) by investigating the subsurface relationship between, and evolution of, concentric thrust faults and the elevated mantle plug beneath several other lunar mascon basins.

## 1.3. Application to Lunar Mascon Basins

Mare Crisium is not the only mascon basin on the Moon to host a basin-concentric network of wrinkle ridges or an annulus of elevated terrain. Other such lunar basins were selected for the study here based on the presence of at least portions of an elevated, bench-like topographic feature delimited on its inner edge by wrinkle ridges. These selected basins—Maria Serenitatis, Nectaris, Humorum, Imbrium, and Mosoviense—are all situated on the lunar near side except for Mare Mosoviense (Figure 1). (Importantly, there are no formal International Astronomical Union-approved names for these basins, and so per convention we refer to those unnamed basins by the named basaltic deposits therein.)

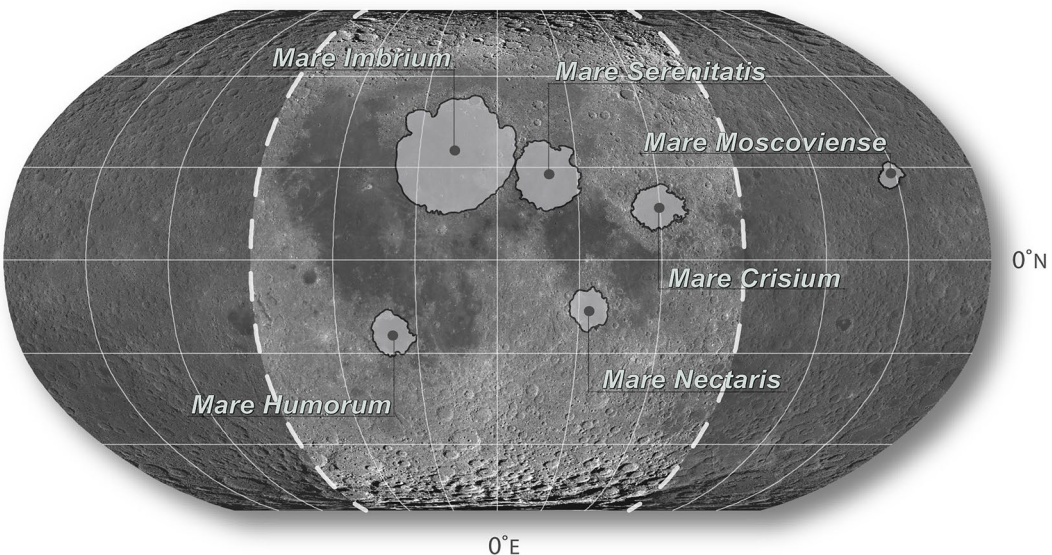


**Figure 1.** A global photogeological image mosaic, in Robinson projection and centered at 0°E, of the lunar surface showing the location of each basin detailed in this study. Dashed white lines of longitude demarcate the boundary between the near- and far-side hemispheres.

The 674 km-diameter basin hosting Mare Serenitatis is adjacent to the southeastern margin of Mare Imbrium (Figure 1) and is likely the oldest (i.e., Pre-Nectarian) such basin we studied, although model ages of the mare deposits are variable (Fassett et al., 2012; Stöffler & Ryder, 2001; Stöffler et al., 2006). An elevated bench parallels the inner basin ring at azimuths of 180°–240°, measured clockwise from the north. Thickness estimates for the basaltic infill within Serenitatis are up to 4.3 km (Williams & Zuber, 1998), although earlier estimates had indicated thicknesses of as much as 10 km (Solomon & Head, 1980). Most of these basalts were emplaced during the Upper Imbrian at approximately 3.8–3.4 Ga (Hiesinger et al., 2000, 2011).

Mare Nectaris (Figure 1) is 340 km across and marks the beginning of the Nectarian (Fassett et al., 2012). As for Serenitatis, Nectaris hosts a partially elevated topographic bench; this bench is most pronounced in the eastern and western parts of the basin. Formation age estimates for Nectaris vary from 3.92 Ga (Stöffler & Ryder, 2001; Stöffler et al., 2006) to  $4.1 \pm 0.1$  Ga (Neukum & Ivanov, 1994). U–Th–Pb dating of samples returned from Apollo 16 showed that at least some of the mare basalts are as old as 3.8 Ga (Maurer et al., 1978). Mare thickness values within Mare Nectaris (0.8 km) are substantially less than those for the other near-side basins detailed in this study, as well as for Mare Crisium (Williams & Zuber, 1998).

Mare Humorum (Figure 1) is the southernmost case study basin and, at 420 km in diameter, is comparable in size to Mare Nectaris. An elevated section of the mare floor is located at 90°–170° azimuth. To the northwest of Humorum, subparallel sets of graben imply that extensional tectonics prevailed outside the basin perimeter (Melosh, 1978; Solomon & Head, 1980). Humorum is intermediate in age between Maria Nectaris and Imbrium (Fassett et al., 2012). In contrast to the other southern-hemisphere basin detailed herein (Mare Nectaris; 0.8 km), the mare basalts in Humorum are considerably thicker at 3.6 km (Williams & Zuber, 1998), likely indicative of thermal heterogeneities within the lunar crust (Solomon & Head, 1980).

Mare Imbrium (Figure 1) is the largest lunar mascon basin, with a diameter of 1,145 km. In addition to its great areal extent, Imbrium is also the geologically youngest of the basins presented herein; its formation marks the start of the Lower Imbrian at ca. 3.85 Ga (Fassett et al., 2012; Stöffler et al., 2006). The most pronounced shortening structures within Imbrium are found at azimuths of 90°–180° and 270°–360°. The basin floor outward of these structures (i.e., toward the basin perimeter) sits at elevations above the corresponding portion in the north; however, a prominent annular bench of elevated topography is lacking at nearly all azimuths. Williams and Zuber (1998) found that the mare thickness within the Imbrium is as much as 5.3 km. Data from the Apollo and Lunar Prospector missions show that Imbrium hosts a higher abundance of KREEP-enhanced rocks—i.e., enriched in potassium (K), rare-earth elements (REEs), and phosphorus (P)—than the other near-side lunar

basins (Lawrence et al., 1998; Wieczorek & Phillips, 2000). This locally high abundance of radiogenic elements likely affected the early thermal and tectonic evolution of Imbrium (Wieczorek & Phillips, 2000).

Mare Moscovense (Figure 1) is the only case study basin located on the lunar far side. Moscovense is highly asymmetric in plan view and much narrower when measured parallel to latitudinal small circles (diameter,  $D = 275$  km) than in its southwest–northeast extent ( $D = 445$  km); the asymmetry of Moscovense may be the result of a double impact (Ishihara et al., 2011). Therefore, to analyze the effect of basin size on the geometric properties of ridge-producing thrust faults, we consider Nectaris as the smallest case study basin ( $D = 340$  km). Relative age chronology of the lunar mare basins suggests that Moscovense formed after the Nectaris basin but before Crisium (Fassett et al., 2012).

This last basin is an important addition to the study because of the substantial difference in crustal and mare thickness between the Moon's near- and far-side hemispheres (Miljkovic et al., 2013). That is, average crustal thickness values are about 15 km greater and the average mare deposits are typically 100–200 m less thick on the lunar far side than on the near side; isolated far-side deposits do exceed 1 km in thickness (Gillis & Spudis, 2000; Wieczorek et al., 2006; Yingst & Head, 1997, 1998, 1999). If our findings for Moscovense are as those for the near-side basins, we will have determined that the process(es) that drive deep-seated thrust faulting are not restricted to the lunar near side. However, the possibility exists that the Moscovense faults are not geometrically similar to those in other basins. If so, then it is likely that the tectonic modification of Mare Moscovense may have been influenced at least in part by having formed within the thicker crust (Wieczorek et al., 2013) on the lunar far side.

Establishing the penetration depth of the bench-bounding ridge faults in each of the basins described above offers information regarding the nature and development of those structures (cf., Byrne et al., 2015). In addition to their penetration depths, determining the spatial relationship between these faults and the elevated crust–mantle interface beneath each basin will provide further insight into the evolution of these basins. If these bench-bounding faults partially or wholly encircle, and are subparallel to, the mascon boundary at depth, then their formation may be similar to that found for Mare Crisium (Byrne et al., 2015) and thus be typical of the evolution of lunar mascon basins in general. Conversely, if the fault architecture found for Crisium is not representative of shortening structures in these other basins, then the formation of such structures is likely more complex than the factors pertinent to Crisium suggest. And, if the fault penetration depths within and between these case study basins vary considerably in otherwise similar structural settings, then the debate of whether wrinkle ridges are thin- or thick-tectonic structures (Golombek et al., 2001; Mangold et al., 1998; Montési & Zuber, 2003; Watters, 1991; Zuber, 1995) may need to be revised into a continuum of faulting depths.

## 2. Methods

We refined and expanded the workflow established for Mare Crisium by Byrne et al. (2015) to several other mascon basins that feature a partial annulus of elevated terrain: Maria Imbrium, Serenitatis, Humorum, Nectaris, and Moscovense.

### 2.1. Mapping

Structural mapping was performed in an ArcGIS® environment at a minimum view scale of 1:200,000. This scale was deemed sufficient to map the primary circumferential shortening structures. Wrinkle ridges were identified with the Lunar Reconnaissance Orbiter Camera wide-angle camera (LROC WAC) global mosaic, which has an equatorial resolution of 100 m per pixel (m/px) (Speyerer et al., 2011). For structures not readily resolvable with LROC WAC imagery, the Lunar Orbiter Laser Altimeter and Kaguya Terrain Camera merged digital elevation model (DEM) (SLDEM2015; Barker et al., 2016), with an equatorial resolution of 59 m/px, were used in conjunction with artificially illuminated shaded-relief maps. Illumination azimuths of 0° and 180° were used to identify east–west-oriented structures, whereas azimuths of 90° and 270° were used to identify north–south-oriented structures.

Shortening structures were identified based on a morphology generally characterized in cross-section by a steeply dipping forelimb (~3°) and tapered backlimb (<1°) (Schultz, 2000), one not related to cratering, ejecta blanketing, or normal faulting. The cross-sectional asymmetry of these structures, however, is variable and likely reflects

**Table 1**

A Summary Table of Fault Parameters Used for Forward Modeling of Lunar Shortening Structures

Parameter (units)	$\delta$ ( $^{\circ}$ )	$d_{\text{top}}$ (km)	$d_{\text{bottom}}$ (km)	$D_{\text{max}}$ (m)
Planar faults				
Range	10–45	0–5	6–60	50–2,000
Increment	1	1	1	50
Listric faults				
Range	10–50	0–5	6–60	50–2,000
Increment	3	3	1	50

*Note.* A total of 386,880 fault configuration files were generated for both homoclinal and listric faults. Fault dip angle ( $\delta$ ), burial depth ( $d_{\text{top}}$ ), penetration depth ( $d_{\text{bottom}}$ ), and maximum fault displacement ( $D_{\text{max}}$ ) were varied for each model iteration. To simulate listric fault geometries, the maximum dip angle was set at the upper fault tip and decreased linearly at five equal depth intervals to a minimum dip angle at the lower fault tip (which had values of  $1^{\circ}$ – $20^{\circ}$ ). For each model iteration, all but one parameter was held constant.

along-strike changes in the geometry of underlying faults; no single morphology consistently characterizes all of these landforms. Each of the investigated basin hosts at least a partial annulus of elevated terrain, the inner edge of which is marked by arcuate wrinkle ridges. These shortening structures are of interest given their approximate collocation with the boundary of the peak free air and Bouguer gravity anomaly values within each basin; gravity data (of degree and order 660) are from the Gravity Recovery and Interior Laboratory (GRAIL) mission (Zuber et al., 2013).

## 2.2. Fault Modeling

A minimum of three ridges were selected in each basin for further modeling based on a relatively preserved morphology with minimal degradation by cratering, subsequent faulting, or ejecta blanketing. Circumferential, bench-bounding structures resembling those in Mare Crisium (Byrne et al., 2015) were preferentially selected. Topographic profiles were extracted perpendicular to the strike of these landforms. Where necessary, these topographic data were detrended to account for regional slope. An elastic dislocation model, Coulomb v3.3 (Okada, 1992; Lin & Stein, 2004; Toda et al., 2005; available online at <https://earthquake.usgs.gov/research/software/coulomb>), was used to generate cross-sectional surface displacement profiles for a variety of fault configurations.

Each individual modeled surface displacement profile was iteratively compared with the observed topography across each of the selected ridges. Because of the relative lack of erosion on the Moon, the relief across each landform is taken to be representative of the vertical component of fault displacement. Horizontal and vertical scaling discrepancies between the modeled and observed topography were corrected by setting the origin of the datum at the inflection point along the crest of each ridge. The root-mean-squared error (RMSE) was calculated to quantify the mismatch between the two profiles. Error calculations were performed across a domain that encompassed the entire morphology of the structure at a sampling interval of 0.5 km; this analysis domain varied as a function of the breadth, or total horizontal extent, of each landform. The model solution with the minimum RMSE value was taken as representative of the fault geometry responsible for producing the observed topography.

We note that the deformation modeled here occurred after the emplacement of the mare file in each basin because of the reactivation of preexisting thrust faults. Indeed, the faults we document here likely accommodated additional slip prior to the emplacement of the final instances of mare basalts, because the stress state responsible for these structures arose immediately after the basin formation (Byrne et al., 2015). It stands to reason, then, that the stress state that led to these thrust faults developing persisted for a considerable amount of geological time.

To address the nonuniqueness of the fault solutions, contour maps were generated with each node representing the minimum RMSE for a particular combination of fault dip angle and fault penetration depth. The fit was deemed satisfactory if only a single region of the parameter space converged on a minimum RMSE value (Figures S3–S7 in Supporting Information S1). A bootstrapping method ( $n = 5,000$ ) was used to calculate the mean fault dip angle and penetration depth across all the best fit modeled fault solutions (Figure S8 in Supporting Information S1).

Fault dip angle ( $\delta$ ), depth of burial ( $d_{\text{top}}$ ), penetration depth ( $d_{\text{bottom}}$ ), and maximum fault displacement ( $D_{\text{max}}$ ) were independently varied for each model iteration. The fault dip angle was varied in  $1^{\circ}$  increments, the fault penetration and fault burial depths in 1 km increments, and the maximum fault displacement in 50 m increments (Table 1). Fault displacement was tapered at the upper, lower, and along-strike fault tips. Each model featured a fixed fault length of 60 km; this fault length was sufficient to avoid edge effects in our 2D models when extracting cross-sections through the center of the resultant model surface displacement. We considered faults with both constant- and variable-dip angles. However, faults were preferentially tested with a homoclinal geometry (i.e., a constant dip angle with depth) to avoid adding complexity to the models. Given the added geometric complication and computational demands of listric fault models, the maximum fault dip angle and fault penetration were

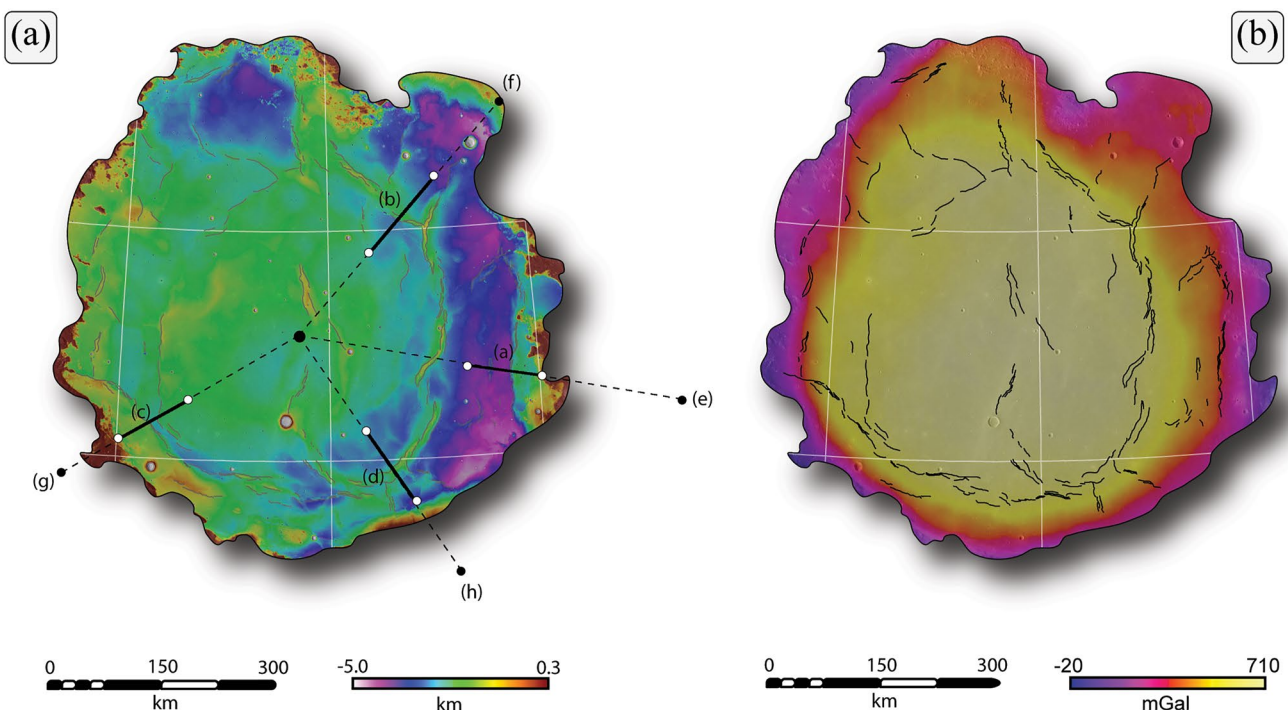


**Figure 2.** The topography from the SLDEM2015 digital elevation model (a) and Bouguer gravity anomaly signature (b) of Mare Serenitatis. Solid black lines (a–d) in panel (a) are lines of section along which elevation values were extracted for use in modeling landforms (Figures 3a–3d). Dashed black lines (e–h) in panel (a) are lines of section along which elevation data and crustal thickness values (Wieczorek et al., 2013) were extracted to visualize the relationship between our modeled fault solutions and the crust–mantle interface (Figures 3e–3h). The solid black lines in panel (b) represent the mapped wrinkle ridges and their spatial relationship with the Bouguer gravity anomaly. These maps are in orthographic projection and are overlaid on the Lunar Reconnaissance Orbiter Camera wide-angle camera global mosaic (Speyerer et al., 2011). All subsequent basin maps are plotted in the same style.

varied in increments of  $3^\circ$  and 3 km, respectively (Table 1). This iterative approach is substantially more robust than previous applications of Coulomb for forward fault modeling (e.g., Byrne et al., 2015), as it allowed us to explore a large parameter space with higher resolution than before.

### 2.3. Crust–Mantle Interface

Elevation values were extracted from the SLDEM2015 DEM (Barker et al., 2016) along radial cross-sections constructed from the center of each basin. Each cross-section was positioned such that it passed through a landform with a modeled fault solution. Crustal thickness values from the GRAIL-derived “Model 1” by Wieczorek et al. (2013) were extracted along this same line of section. The approximate depth to the crust–mantle interface beneath each basin was determined by subtracting crustal thickness values from the elevation values, after Byrne et al. (2015). The best-fit modeled fault solutions were superposed on the crust–mantle interface model to assess the geometric and spatial relationship between these faults at depth and the elevated mantle plug beneath each basin.

## 3. Results

### 3.1. Mare Serenitatis

#### 3.1.1. Structural Mapping and Gravity Signature

Mare Serenitatis (Figure 2) hosts a near-encircling set of basin-circumferential ridges. The vertical offset (assumed to be directly manifest as the topographic relief in the absence of major erosion on the Moon) and breadth of these landforms vary along the strike, but generally these features have 200–400 m of relief. Broader structures, located at azimuths of  $80^\circ$ – $100^\circ$  and  $170^\circ$ – $240^\circ$ , mark the inner edge of an annular bench of elevated topography. Another set of narrower landforms parallel to the elevated bench in the eastern portion of Serenitatis is situated

**Table 2**

A Summary Table of Best-Fit Modeled Fault Solutions for Each Mascon Basin: Maria Serenitatis, Nectaris, Humorum, Imbrium, and Moscovense

Structure	Fault type	Dip angle (°)	Penetration depth (km)	Burial depth (km)	Maximum fault displacement (m)	RMSE (m)
Mare Serenitatis						
(a)	Planar	21	20	<1	300	15
(b)	Planar	16	19	1	350	13
(c)	Planar	16	28	<1	750	19
(d)	Planar	12	14	4	450	14
Mare Nectaris						
(a)	Planar	12	25	5	950	38
(b)	Planar	18	21	4	650	19
(c)	Planar	28	29	5	400	15
Mare Humorum						
(a)	Planar	18	13	2	500	16
(b)	Planar	21	10	2	350	16
(c)	Listric	20 → 1	6	2	350	18
(d)	Listric	40 → 5	9	1	150	6
Mare Imbrium						
(a)	Planar	42	14	3	500	28
(b)	Planar	10	47	2	1,050	33
(c)	Planar	11	16	3	800	15
(d)	Planar	36	10	2	550	32
Mare Moscovense						
(a)	Planar	26	51	<1	950	32
(b)	Planar	26	17	<1	300	17
(c)	Planar	45	7	1	100	6
(d)	Planar	35	17	<1	200	15

Note. A minimum of three model solutions is shown for each basin. Visual representations of the best fit model solutions are shown in Figures 3–6 and Figures 8–11. The “→” symbol indicates a listric fault geometry, where the fault dip angle decreases from a maximum value at the upper fault tip to a minimum at the lower fault tip.

about 100 km toward the basin interior. Several north–south-oriented structures with <200 m relief extend across the center of the basin.

Typically, wrinkle ridges within Mare Serenitatis are asymmetric in cross-section. The interpreted vergences (or the direction of tectonic transport) of the asymmetric folds overlying the causal thrust faults, however, does vary along the strike. In the northwestern part of Serenitatis, ridges are either limited in their topographic expression or are completely absent.

Importantly, inward-verging structures within Mare Serenitatis approximately delineate the boundary of the peak-positive Bouguer gravity anomaly values (Figure 2b). As for Crisium (Byrne et al., 2015), these ridges tend to be subparallel to this boundary and are slightly offset from the maximum gravity gradient toward the basin interior. The morphological similarities between Maria Crisium and Serenitatis strongly suggest that a fault architecture similar to that demonstrated for Crisium (Byrne et al., 2015) also exists in this basin.

### 3.1.2. Modeling Results and Subsurface Geometry

Four basin-circumferential ridges representative of many of the structures seen in Serenitatis are presented here (Table 2, Figure 3). This subset of wrinkle ridges is indicative of outward-dipping faults (Figure 3) that are collocated with the boundary of the maximum positive Bouguer gravity anomaly in the basin (Figure 2). Best-fit model solutions suggest that the thrust faults responsible for these landforms are shallowly (<4 km) buried beneath the lunar surface and penetrate to depths of 14–28 km (Figures 3a–3d). The dip angle of these faults is never more than 21° (Table 2). However, a satisfactory fit can be produced with dip angles that vary by as much as 10° from the best-fit solution. Despite uncertainty in the exact geometric attributes of these faults, this elastic dislocation modeling approach reliably reproduces the landforms observed in Serenitatis and shows that these thrust faults penetrate substantially beyond the base of the mare infill (4.3 km; Williams & Zuber, 1998).

Modeled fault solutions were superposed on a model of the crust–mantle boundary beneath Serenitatis (Figures 3e–3h). These results show that an outward-dipping thrust ring-fault system bounds the superisostatic mantle plug, at least at azimuths of 0°–260° (Figures 2 and 3). This geometric arrangement indicates that, as for Mare Crisium (Byrne et al., 2015), the isostatic adjustment of this superisostatic mantle material acted to localize stresses along the crust–mantle boundary during and after the basin formation.

## 3.2. Mare Nectaris

### 3.2.1. Structural Mapping and Gravity Signature

Ridges mapped for Mare Nectaris tend to be somewhat obscured by ejecta from several adjacent 100 km-diameter craters, including Theophilus, Cyrillus, and Catharina, which has locally blanketed the deformed mare infill (Figure 4a). This tempering of morphology is most evident along the northwestern basin perimeter, where the topographic expression of crustal shortening is all but absent. If shortening structures did exist in the northwest of Nectaris, any evidence of such is masked by the Moon's long impact history; this ejecta material does not show any sign of being tectonically deformed.

A bench of elevated terrain was found at azimuths of 0°–160° and 200°–290°. Along the eastern perimeter of the basin, this arcuate bench is marked by wrinkle ridges along the inner edge (Figure 4a). In the west–southwest region of the basin, however, ridges are less pronounced and are frequently veiled by ejecta deposits.

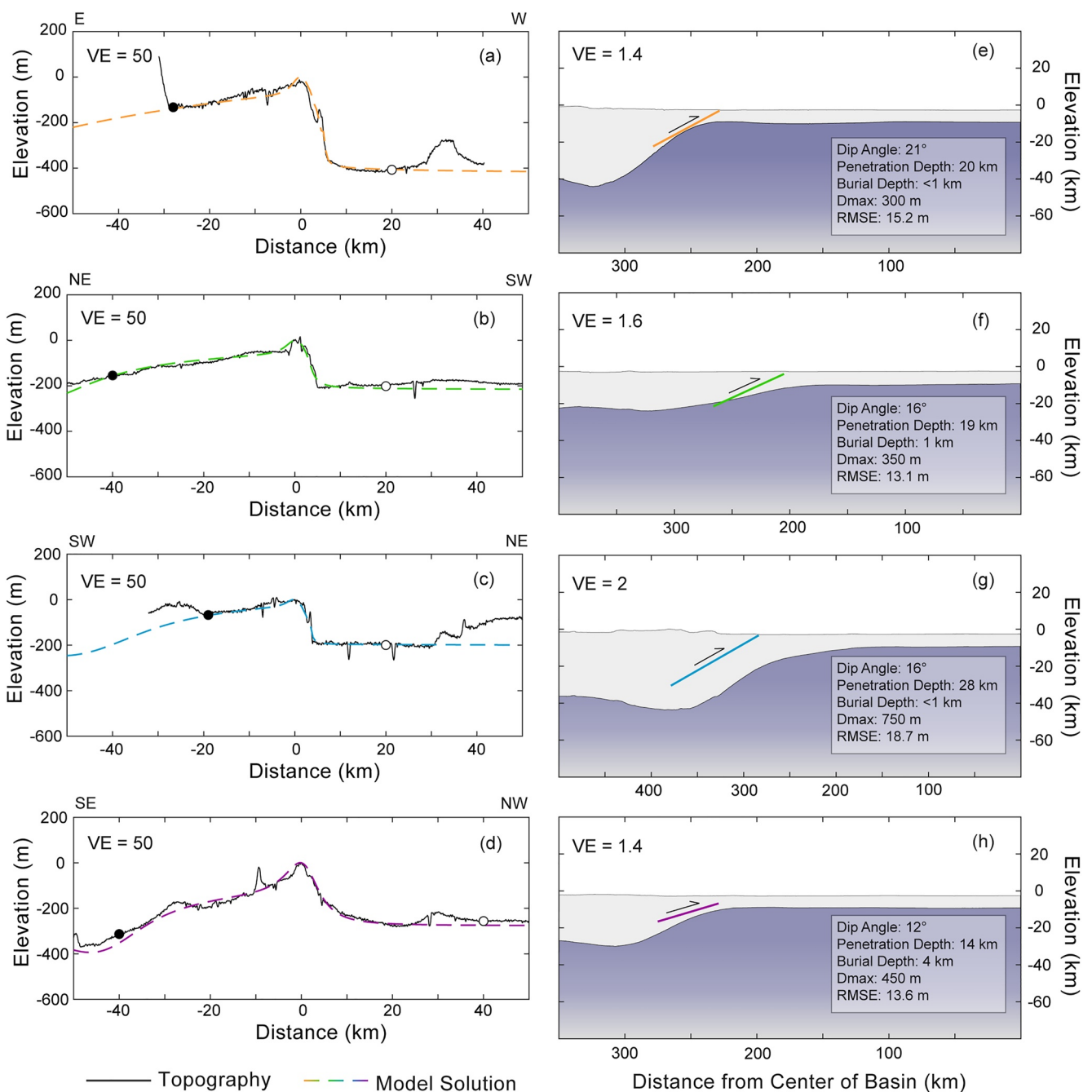


**Figure 3.** Model solutions are shown for four landforms within Mare Serenitatis (a–d; Figure 2a), along with the corresponding crust–mantle model depicting the geometric relationship between the best-fit fault solution and the elevated mantle plug (e–h; Figure 2a); the crust is depicted in light gray, whereas the mantle is shown with a dark slate-blue gradient. Root-mean-squared error (RMSE) values were calculated for the domain bounded by the black (start) and white (finish) circles along each cross-section (a–d).

At azimuths of  $080^\circ$ – $170^\circ$  and  $200^\circ$ – $280^\circ$ , the maximum positive Bouguer gravity gradient is clearly demarcated by wrinkle ridges (Figure 4b). These ridges are typically situated 20–30 km inward from the boundary of the peak-positive Bouguer gravity anomaly. This spatial pattern resembles that observed for Crisium and Serenitatis and provides qualitative evidence for a similar geometry of outward-dipping thrust faults bounding the elevated mantle plug beneath the Nectaris basin.

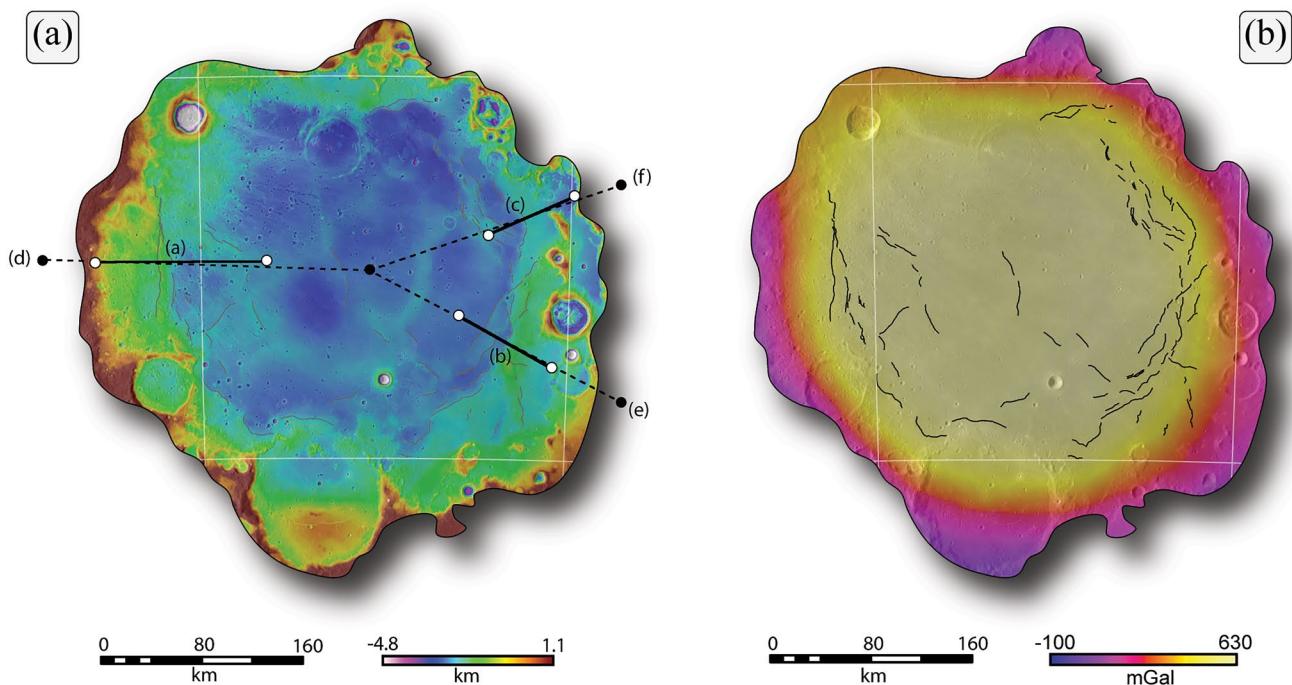


**Figure 4.** The topography from the SLDEM2015 digital elevation model (a) and Bouguer gravity anomaly signature (b) of Mare Nectaris. Profiles from the lines of section in panel (a) are shown in Figure 5. The symbology and display of data sets are as for Figure 2.

### 3.2.2. Modeling Results and Subsurface Geometry

The proximity of several large, adjacent craters impeded our forward modeling approach by reducing the number of ridges with a sufficiently preserved morphology for this analysis. Three ridges along the perimeter of Mare Nectaris at azimuths of 060°, 130°, and 270° were selected for modeling (Figures 4 and 5). Each of these landforms marks the inner edge of an arcuate portion of the elevated terrain. The cross-sectional relief (250–500 m) and general morphology of these structures are broadly similar, featuring only minor variations. However, there is substantial variability in the fault dip angle and penetration depth required to reproduce the landform in Figure 5a. This variability is likely the result of modification by impacting and a less pristine morphology, as well as the truncated backlimb (see Supporting Information). Despite the inconsistent surficial characteristics of the resultant landforms, the geometric attributes, particularly the penetration depth, of the underlying thrust faults are relatively uniform (Table 2, Figure 5). The fault dip angles suggested by the model solutions range from 12° to 28°; the model penetration depths are 21–29 km. The average burial depth of faults within Nectaris is greater than that found for Crisium (Byrne et al., 2015) and for Serenitatis (Table 2).

These modeled fault solutions demonstrate that radially outward dipping thrust faults along the perimeter of Mare Nectaris, at least along its eastern and western boundaries, are subparallel to the crust–mantle interface at depth (Figures 4 and 5d–5f). The structure located at an azimuth of 270° dips more shallowly (12°) than the boundary of the elevated mantle plug; this finding may be the result of the degraded nature of this landform, as acceptable fits can be obtained with fault dip angles of 10°–27° (illustrating the limitations of this modeling approach). Regardless of the geometric variability, these results show that, as for Crisium and Serenitatis, an outward-dipping thrust ring-fault system bounds at least a portion of the elevated mantle plug beneath Nectaris.

## 3.3. Mare Humorum

### 3.3.1. Structural Mapping and Gravity Signature

Mare Humorum, adjacent to the southern extent of Oceanus Procellarum (Figure 1), hosts an arcuate portion of elevated topography at azimuths of 90°–170° and is generally delimited by wrinkle ridges (Figure 6a). These structures typically have <300 m of relief and their morphology suggests that underlying thrust faults dip away

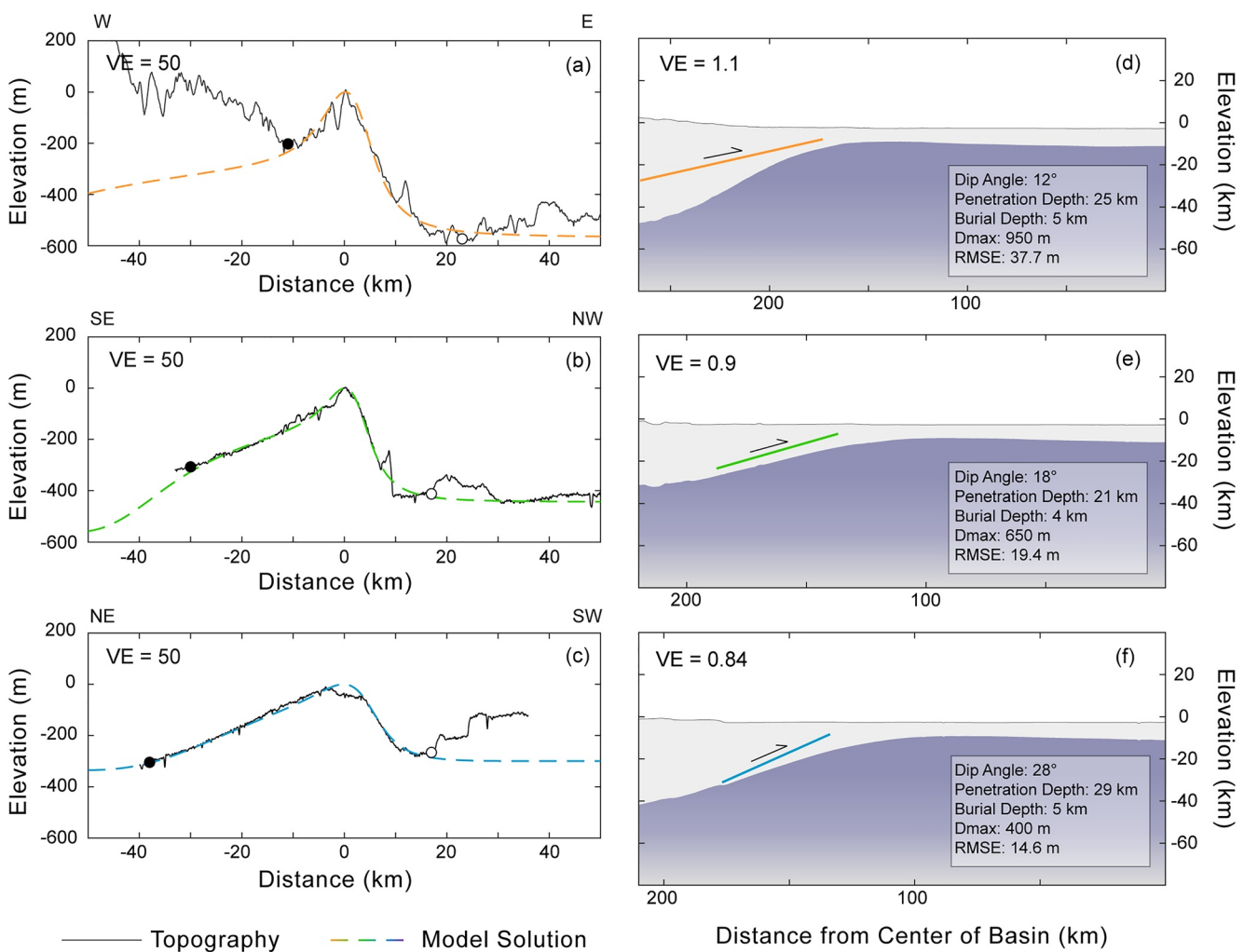


**Figure 5.** Model solutions are shown for four landforms within Mare Nectaris (a–c; Figure 4a), along with the corresponding crust–mantle model depicting the geometric relationship between the best fit fault solution and the elevated mantle plug (d–f; Figure 4a). Root-mean-squared error (RMSE) values were calculated for the domain within the black (start) and white (finish) circles along each cross-section (a–c).

from the basin interior. As at Mare Nectaris (Figure 4), shortening structures are absent along the western–northwestern boundary of Humorum, although a topographic bench is present (Figure 7a). It is possible that blind thrust faults outside our parameter range underlie the bench in this portion of the basin. A set of rilles or grabens has formed in the adjacent highlands as a result of crustal extension (Solomon & Head, 1980).

In the eastern portion of Humorum, three distinct sets of ridges are evident, and each is subparallel to the basin boundary. The innermost of these lineaments is offset by 50–70 km from the outermost, bench-bounding ridges. Ridges located at azimuths of 0°–170° are more pronounced than those along the southwestern perimeter of Humorum, where the tectonic regime seemingly transitions from compressional to extensional. As for the other basins on the lunar near side, scattered wrinkle ridges within the interior of Mare Humorum have a preferential north–south orientation (Figure 6).

The positive Bouguer gravity anomaly signature within Mare Humorum mirrors the geometry of the basin itself and, where such structures are present, is delimited by wrinkle ridges (Figure 6b). As before, these ridges are typically located several tens of km from the boundary of this maximum positive Bouguer gravity anomaly toward the basin interior. Wrinkle ridges parallel to the eastern boundary of the basin are situated inward of the outer edge of the maximum gravity anomaly values by as much as 100 km. Curiously, this gravity signature also parallels the basin boundary along the northwestern perimeter of Humorum, where only extensional tectonic structures are present (Figure 6).

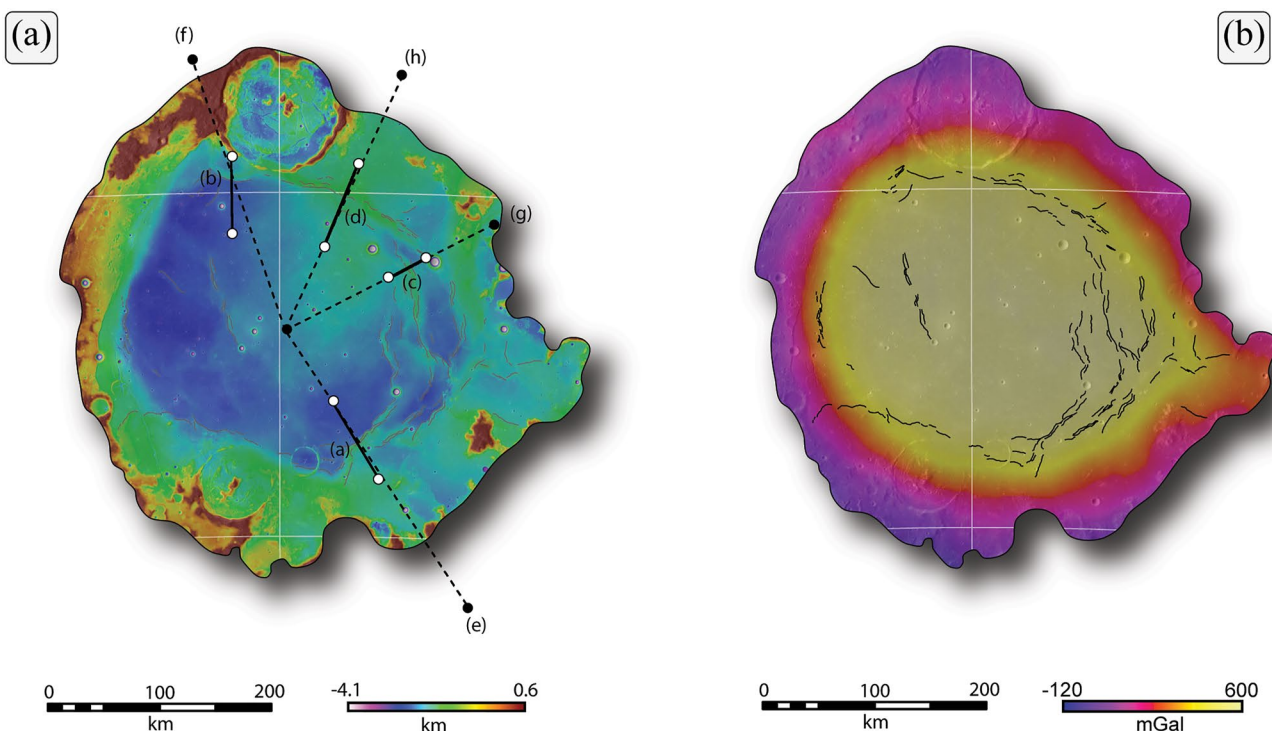


**Figure 6.** The topography from the SLDEM2015 digital elevation model (a) and Bouguer gravity anomaly signature (b) of Mare Humorum. Profiles from the lines of section in panel (a) are shown in Figure 7. The symbology and display of data sets are as for Figure 2.

### 3.3.2. Modeling Results and Subsurface Geometry

Four landforms (Table 2) at azimuths of  $010^\circ$ – $160^\circ$  and  $350^\circ$  were selected for modeling (Figure 7) based on their approximate collocation with the boundary of the maximum positive Bouguer gravity anomaly within Mare Humorum (Figures 6 and 7). One such ridge (Figure 7c), situated along an isolated belt of similar structures, is found about 50 km from the elevated bench to the west (Figure 6; see Section 3.3.1). This structure was selected to characterize further the relationship between these lineaments which, in plan view, are subparallel to the basin boundary and maximum gravity gradient.

Three of the landforms have similar geometric attributes, although one structure required a listric model fault geometry to achieve a satisfactory model fit (Table 2). The homoclinal fault solutions at azimuths of  $160^\circ$  and  $350^\circ$  are nearly identical, having dip angles of  $18^\circ$ – $21^\circ$  and penetrating 10–13 km into the lunar lithosphere (Table 2, Figures 7a and 7b). The ridge located at an azimuth of  $010^\circ$  requires a listric model fault geometry with a maximum dip angle of  $40^\circ$  at the upper fault tip and a minimum dip angle of  $5^\circ$  at the lower fault tip; the modeled fault solution suggests a fault penetration depth of 9 km (Figure 7d). Each of these faults dips away from the center of Humorum.

A listric fault geometry was necessary to obtain a satisfactory fit for the structure at a bearing  $060^\circ$  (Table 2, Figure 7c). This best fit fault solution has a maximum dip angle of  $20^\circ$  at the upper fault tip and terminates subhorizontally at a depth of 6 km (Figure 7c), approximately 2 km below the estimated base of the mare infill (Williams & Zuber, 1998). In contrast to every other structure detailed in this study, this fault appears to dip *toward* the basin interior. This landform does not delineate a topographic bench, although elevated terrain is present farther toward the edge of the basin.

The outward-dipping thrust faults within Mare Humorum (Figures 7a, 7b and 7d) are all subparallel to the boundary of the elevated mantle plug beneath the basin (Figures 7e, 7f and 7h). However, faults at Humorum penetrate to shallower depths (<13 km) than those within the basins detailed above. Although it appears that a partial thrust ring-fault system approximately bounds the crust–mantle interface beneath the basin, this arrangement is only evident at azimuths of  $010^\circ$ – $170^\circ$  and  $350^\circ$  (Figures 6 and 7). The exact down-dip geometry of these faults varies along the strike.

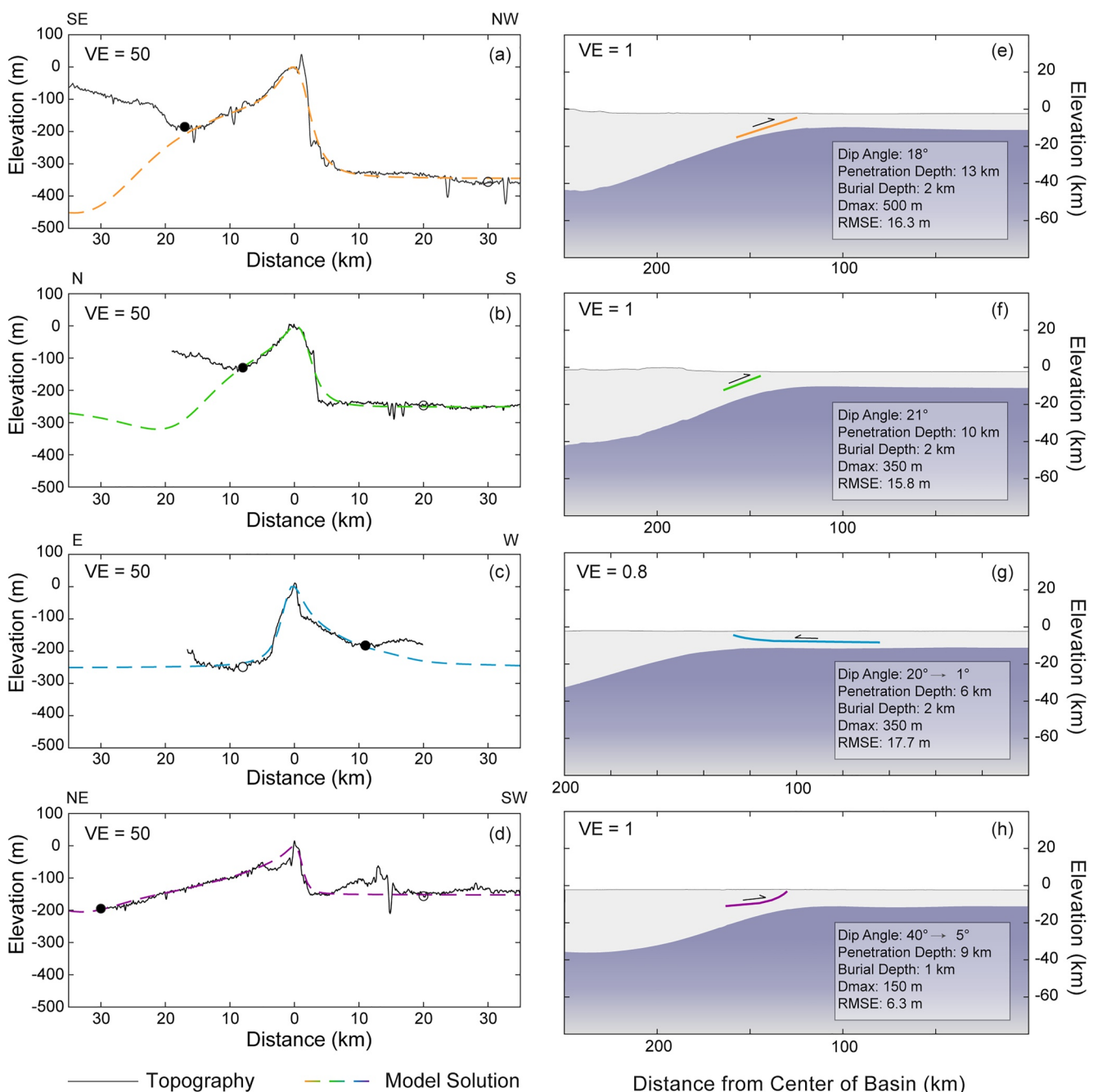


**Figure 7.** Model solutions are shown for four landforms within Mare Humorum (a–d; Figure 6a), along with the corresponding crust–mantle model depicting the geometric relationship between the best fit fault solution and the elevated mantle plug (e–h; Figure 6b). Root-mean-squared error (RMSE) values were calculated for the domain within the black (start) and white (finish) circles along each cross-section (a–d).

### 3.4. Mare Imbrium

#### 3.4.1. Structural Mapping and Gravity Signature

As for Maria Crisium and Serenitatis, a near-circumferential set of shortening structures is present within the perimeter of Mare Imbrium. Wrinkle ridges are found at all azimuths along the basin perimeter and comprise a network of landforms that stretches over 5,000 km in length (Figure 8). These structures do not appear to form with any preferential orientation nor do they have a consistent morphology. Ridges that strike east–west typically have a higher degree of cross-sectional asymmetry than the narrower structures that strike north–south.

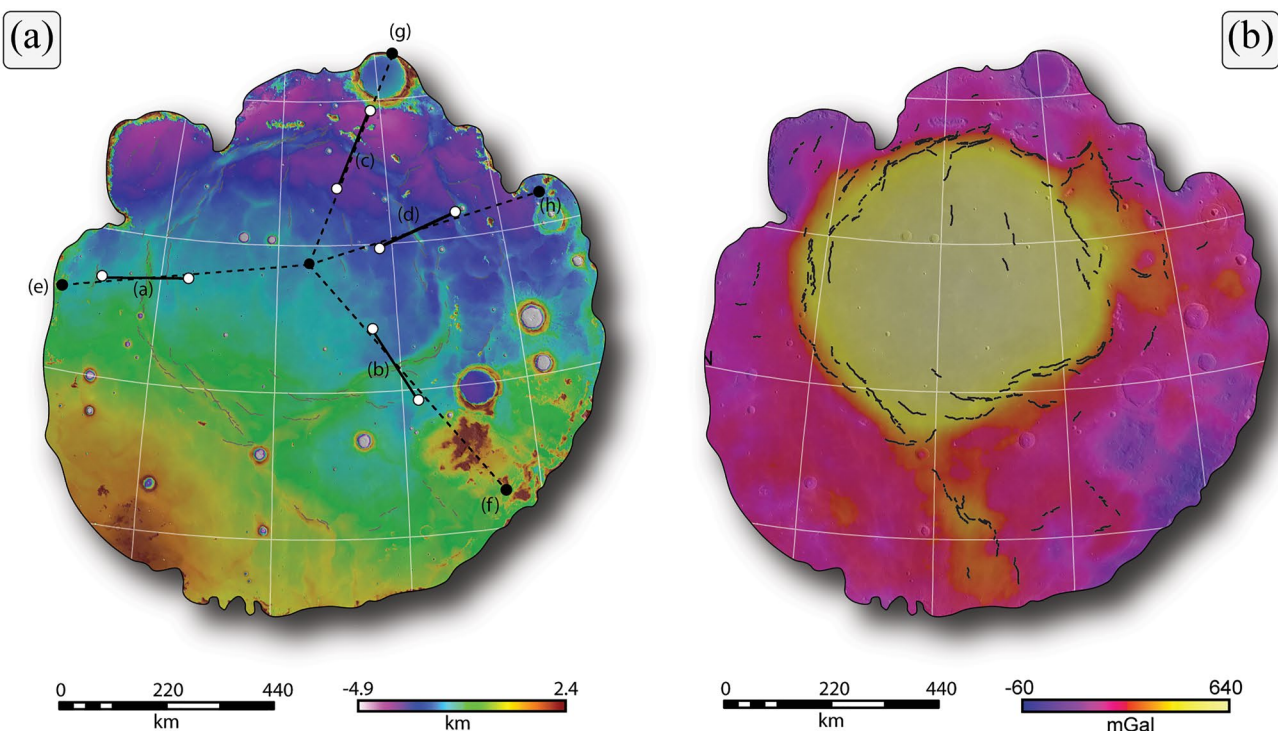


**Figure 8.** The topography from the SLDEM2015 digital elevation model (a) and Bouguer gravity anomaly signature (b) of Mare Imbrium. Profiles from the lines of section in panel (a) are shown in Figure 9. The symbology and display of data sets are as for Figure 2.

In contrast to the other near-side basins detailed above, Imbrium does not host a prominent bench of elevated topography anywhere. Tectonic structures are absent within the interior of the basin (Figure 8). In addition to its vast size ( $>1,000$  km diameter), the regional slope across the north–south extent of Imbrium is higher than any other mare basin (Figure 8).

Basin-circumferential structures within the Imbrium typically outline the boundary of the maximum-positive Bouguer gravity anomaly (Figure 8b). This collocation is evident even in the absence of an elevated topographic bench. As shown for several other mare basins, these ridges are typically situated tens of kilometers inside the boundary of the maximum positive Bouguer gravity signature within the Imbrium.

### 3.4.2. Modeling Results and Subsurface Geometry

Four ridges with variable relief, breadth, and asymmetry were selected for modeling based on their approximate collocation with the maximum gravity gradient within Mare Imbrium (Table 2, Figure 8). The morphology of these structures varies by azimuth, with broader, more cross-sectionally asymmetric structures seen in the north and south but narrower, approximately symmetric structures are in the east and west of Imbrium.

The narrow, relatively high-relief (400–500 m) structures in eastern and western Imbrium are shown to be the product of more steeply dipping faults that are buried several km beneath the lunar surface (Figures 9a and 9d). Shallowly dipping thrust faults are responsible for producing the broader, bench-bounding structures along the northern and southern perimeter of Imbrium (Figures 9b and 9c). The structure shown in Figure 9b penetrates to a far greater depth (30–55 km) than any of the faults detailed for Imbrium, or any of the other near-side lunar basins; the best-fit model solution suggests a fault penetration depth of 47 km.

Apart from the outward-dipping thrust fault at an azimuth of  $150^\circ$ , the faults responsible for generating circumferential wrinkle ridges within Mare Imbrium do not closely parallel the crust–mantle boundary at depth (Figures 9e–9h). Thrust faults underlying the broad, bench-bounding structures in northern and southern Imbrium do tend to more closely follow this interface at depth (Figures 9f and 9g). However, modeled fault solutions for landforms along the eastern and western boundary of Imbrium do not appear to match the geometry found for thrusts and uplifted mantle plugs in the other basins considered here (Figures 9e–9h).

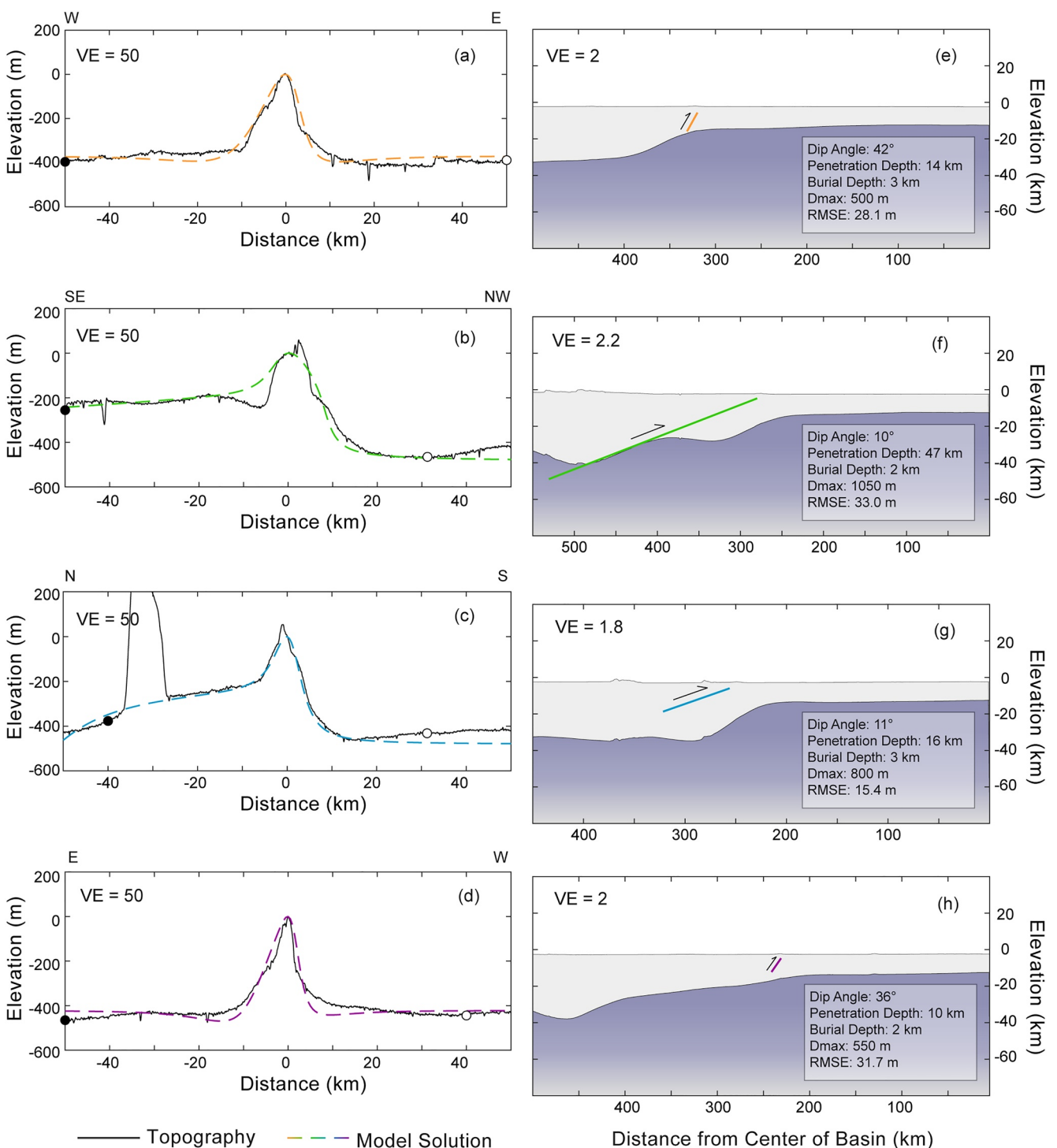


**Figure 9.** Model solutions are shown for four landforms within Mare Imbrium (a–d; Figure 8a), along with the corresponding crust–mantle model depicting the geometric relationship between the best-fit fault solution and the elevated mantle plug (e–h; Figure 8a). Root-mean-squared error (RMSE) values were calculated for the domain within the black (start) and white (finish) circles along each cross-section (a–d).

### 3.5. Mare Mosoviense

#### 3.5.1. Structural Mapping and Gravity Signature

Mare Mosoviense, the only far-side, mascon-bearing basin in this study, hosts ridges with locations and morphologies that compare well with those in near-side basins in that they typically mark the inner edge of

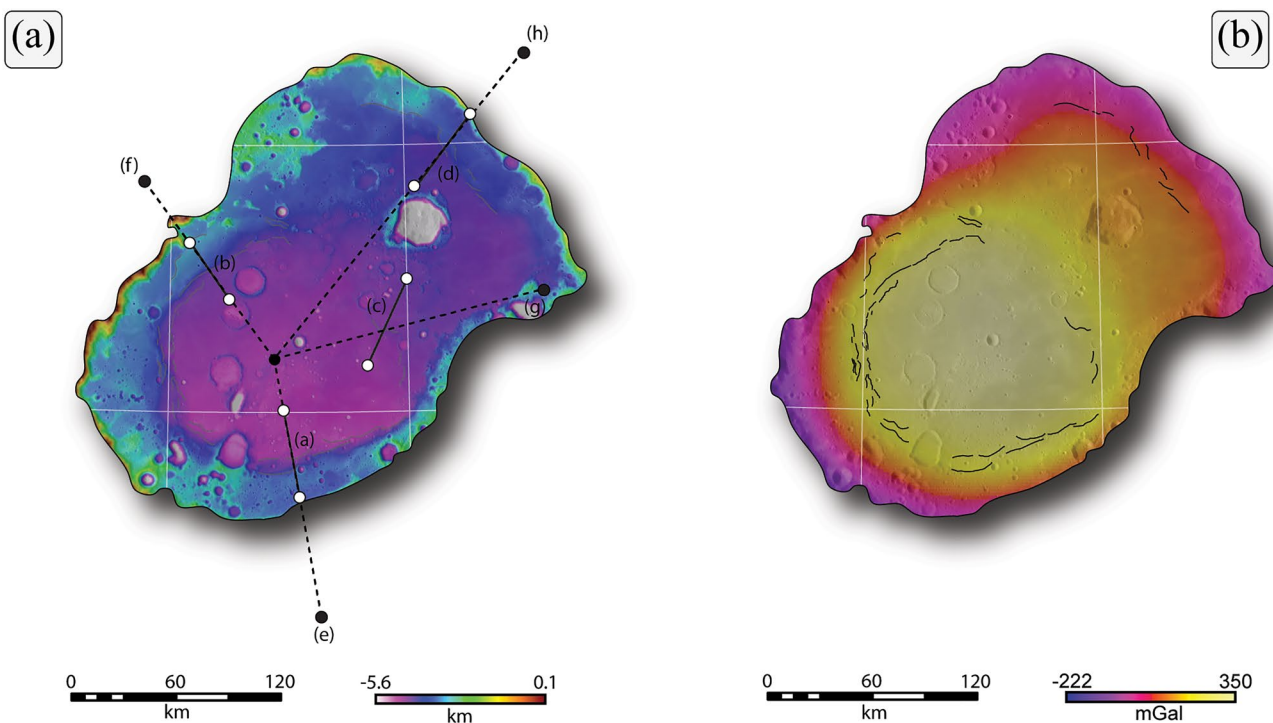


**Figure 10.** The topography from the SLDEM2015 digital elevation model (a) and Bouguer gravity anomaly signature (b) of Mare Moscovense. Profiles from the lines of section in panel (a) are shown in Figure 11. The symbology and display of data sets are as for Figure 2.

a topographically elevated bench. The backlimbs of these ridges are frequently terminated by the basin rim (Figure 10). Basin-concentric elevated terrain and the associated wrinkle ridges are evident at nearly all azimuths in Moscovense. The distribution of mare deposits in the basin is highly asymmetric in plan view. In the northeast, the topographic bench is situated approximately 100 km from the central basin, whereas the elevated terrain at azimuths of 130°–360° defines the inner ring of central Moscovense (Figure 10a). The gravity anomaly signature for Moscovense mirrors this topographic pattern (Figure 10b).

Ridges within Moscovense are relatively contiguous along the basin perimeter. The interior of the basin, much like those on the lunar near side, records limited evidence of tectonic shortening (Figure 10) but instead hosts a series of floor-fractured and buried craters. The relief across the perimeter-parallel shortening structures ranges between <100 and >700 m. Landforms with this much relief are not found in any of the near-side mare basins. As is shown for each of the basins detailed previously, wrinkle ridges—which in Moscovense are nearly ubiquitously bench-bounding—are approximately collocated with the edge of the maximum positive Bouguer gravity anomaly (Figure 10b). As such, structural mapping of the basin supports the proposition that the faults responsible for these shortening landforms do indeed bound the underlying mascon.

### 3.5.2. Modeling Results and Subsurface Geometry

Four tectonic landforms were selected for Coulomb modeling, three of which demarcate the inner edge of the elevated terrain (Table 2, Figure 11). One structure, located within the interior of Moscovense, was selected because of its collocation with the boundary of the peak gravity anomaly values within the basin (Figures 10 and 11). The positive Bouguer gravity anomaly, however, continues outboard of this structure to the northeast, albeit with lower values (Figure 10b).

Modeled fault solutions indicate that the thrust faults responsible for producing bench-bounding ridges within Moscovense typically penetrate to depths greater than 15 km (Figure 11a, 11b and 11d). One such structure, with nearly 800 m of relief, needed a modeled fault solution penetrating to substantially greater depths (51 km; Figure 11a). The best-fit model solution for the shortening landform within the interior of the basin shows that

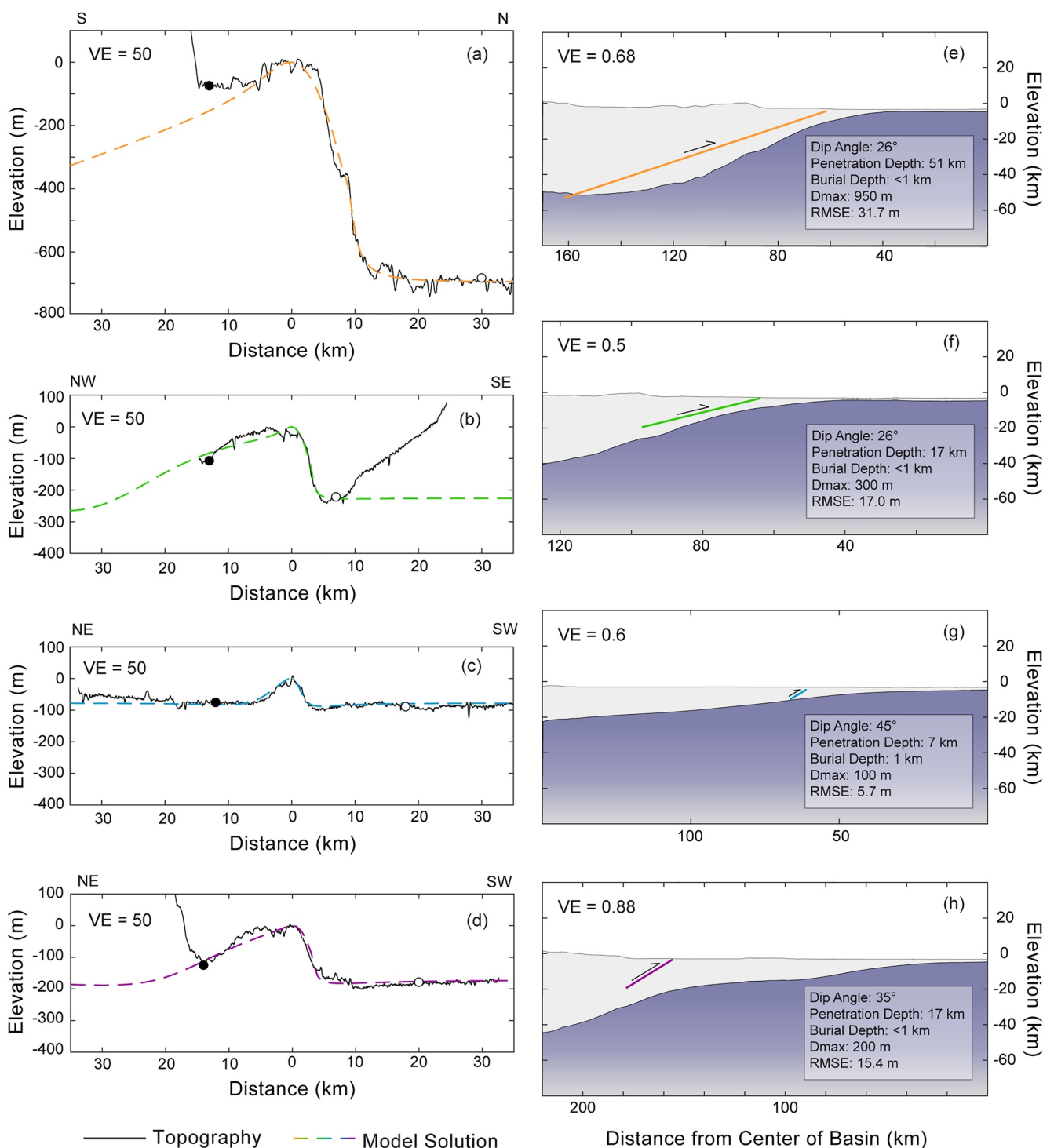


**Figure 11.** Model solutions are shown for four landforms within Mare Moscovense (a–d; Figure 10a), along with the corresponding crust–mantle model depicting the geometric relationship between the best-fit fault solution and the elevated mantle plug (e–h; Figure 10b). Root-mean-squared error (RMSE) values were calculated for the domain within the black (start) and white (finish) circles along each cross-section (a–d). Fault apparent dip ( $38^\circ$ ) is shown in panel (g).

this thrust fault is much shallower, extending only to a depth of 7 km (Figure 11c). This calculated fault penetration depth value is comparable to that of the structure located within the interior of Mare Humorum (Figure 7c).

As for several near-side mascon basins, that is, Maria Crisium, Serenitatis (Figure 3), Nectaris (Figure 5), and, to some degree, Humorum (Figure 7), the modeled fault solutions for Mare Moscovense penetrate substantially below the base of the mare infill (Williams & Zuber, 1998) and tend to coincide with the boundary of the elevated mantle plug (Figures 11e, 11f and 11h). The exception to this geometric arrangement is in the case of the shallowly penetrating fault responsible for the Moscovense interior ridge mentioned above (Figure 11g). There does not appear to be any difference between the fault architecture shown for Moscovense and the near-side basins in this study.

#### 4. Discussion

Each analyzed basin hosts a topographically elevated bench, although this uplifted terrain is typically discontinuous and only encircles a portion of a given mascon basin. The inner edge of this elevated bench, where present, is typically but not always demarcated by wrinkle ridges (Figures 2, 4, 6, 8 and 10). Basin-concentric wrinkle ridges are also present in cases where such elevated, arcuate portions of topography are absent; this is particularly evident for Mare Imbrium. These ridges are collocated with the boundary of the peak-positive Bouguer gravity anomaly values in each basin, albeit to varying degrees; wrinkle ridges and the associated bench, where present, are typically situated  $<50$  km from this boundary toward the basin interior (Figures 2, 4, 6, 8 and 10). These landforms, which deform the mare basalts within each basin, likely started to form immediately after the initial basin formation but remained active, at least intermittently, thereafter in response to the continued loading of basalt.

Thrust faults within the lunar mare basins exhibit a range of penetration depths with variable dip angles and dip directions (Table 2). These faults typically penetrate to depths greater than 10 km and dip radially outward, that is, away from the basin interior. The results of our bootstrapping method ( $n = 5,000$ ) used to determine the mean fault penetration depth and dip angle for best-fit modeled faults indicate that the average faulting depth across all the case study basins is  $22 \pm 3$  km, with a fault dip angle of  $25^\circ \pm 2^\circ$ ; these values do not, however, account for errors intrinsic to individual modeled fault solutions (Figure S8 in Supporting Information S1). In general, though, the faults responsible for basin-circumferential wrinkle ridges within the lunar mascon basins dip radially outward and penetrate to considerably greater depths than the base of the mare infill.

In the case of Maria Serenitatis (Figure 3), Nectaris (Figure 5), Moscovense (Figure 11), and, to a lesser extent, Humorum (Figure 7) and Imbrium (Figure 9), outward-dipping thrust faults are subparallel to the crust–mantle boundary at depth. As shown by Byrne et al. (2015) for Mare Crisium, compressional stresses are concentrated along this interface by the subsidence of the superisostatic mantle plug and uplift of the subisostatic crustal collar encircling the basins. The attempted isostatic adjustment of the heterogeneous lunar lithosphere results in the formation of a (partial) mascon-bounding ring-fault system (Zuber et al., 2016). It is notable that, despite the substantial difference in crustal (Wieczorek et al., 2013) and mare thicknesses (Wieczorek et al., 2006) between the lunar near and far sides (Miljkovic et al., 2013), mascon-bounding thrust ring-fault systems are found for basins in both near- and far-side hemispheres. This geometric arrangement is absent in the northwestern quadrant of the Maria Nectaris and Humorum, as well as for most of the Mare Imbrium, suggesting that some combination of variables—that is, timing of basin formation, local heat flux, and effective elastic thickness—likely impeded strain localization along the crust–mantle interface in those instances.

##### 4.1. Ring Faults on the Earth and Moon

Geometrically comparable structures, albeit on a much smaller scale and with substantially steeper fault dip angles, have been the subject of studies focused on the dynamics of caldera collapses (Acocella, 2006, 2007; Burchardt & Walter, 2010; Geyer & Martí, 2014; Levy et al., 2018). The formation of outward-dipping reverse ring faults is a kinematic consequence of caldera subsidence and collapse. It has been found that, if these ring faults are upward propagating (that is, they nucleate near the magma chamber and propagate toward the surface), then magma transport is possible very early in caldera subsidence (Burchardt & Walter, 2010). Despite the difference in scale, the dynamics allowing for the initiation of reverse slip along radially outward-dipping ring faults are analogous to what was found for Mare Crisium (Byrne et al., 2015). It is possible, then, that these faults acted as magma conduits and helped facilitate the emplacement of the mare basalts, at least for a time; magma transport

along these ring faults would vary temporally due to their stress state, as they must be critically stressed for such transport to occur (Burchardt & Walter, 2010).

Although not included in the study basins presented herein, ring-fault systems have been proposed for Orientale Basin with steeply inward-dipping normal faults ( $60^{\circ}$ – $71^{\circ}$ ) that define the outer crater rings that extend to or into the mantle (Andrews-Hanna et al., 2018; Zuber et al., 2016). Shallowly dipping faults ( $13^{\circ}$ – $22^{\circ}$ ) suggested for the northeastern quadrant of Orientale have been interpreted as normal faults despite geometrically resembling those identified for Mare Crisium (Andrews-Hanna et al., 2018; Byrne et al., 2015), as well as those presented above (see Section 3). The localization of shear along structures resembling ring faults has been predicted by hydrocode modeling, with faults penetrating well into the mantle (Johnson et al., 2016; Potter, 2015; Potter et al., 2013). In the case of the Orientale ring faults, these structures likely formed within several minutes after basin excavation (Johnson et al., 2016; Nahm et al., 2013). Similarly, the structures detailed herein and for Mare Crisium (Byrne et al., 2015) likely began to form immediately after the basin-forming impact. The deformation modeled with our approach, however, came after the maria were emplaced and solidified, such that these structures could express relief. It follows, then, that these faults, which formed soon after impact, remained active throughout and after mare emplacement. Previous studies on the Oriental basin focused on the formation of the outer basin rings and inward-dipping normal faults. Our results for several large impact basins (primarily those hosting Maria Serenitatis, Nectaris, and Moscovense, but also the basins in which Maria Humorum and Imbrium are situated) demonstrate that thrust ring faults are topographically expressed as basin-concentric wrinkle ridges that frequently demarcate an elevated topographic bench; slip along these thrusts takes place either continuously or intermittently throughout and after mare emplacement. It is therefore possible that the shallowly dipping faults identified by Andrews-Hanna et al. (2018) accommodate reverse slip. Future work should further elucidate the nature of ridge-producing faults in the Oriental basin and elsewhere.

The fact that this fault architecture is found within several lunar basins implies that this structural outcome is characteristic of the evolution of large, volcanically infilled mascon basins in general. This outcome is most clearly expressed at Mare Serenitatis (Figure 3) and Mare Nectaris (Figure 5), where outward-dipping thrust faults penetrate to depths  $>20$  km and bound the elevated mantle plug beneath each basin, just as was found for Mare Crisium by Byrne et al. (2015). Under the assumption that this fault architecture develops as has been proposed for Crisium, then the differential vertical motion of a subisostatic crustal collar and superisostatic mantle plug concentrated stress along the crust–mantle interface, driving the formation of these deep-seated faults and the portions of arcuate, elevated, and ridge-bounded topography within each basin. Continued loading of the lunar lithosphere by mare basalts likely provided the additional differential stress to drive repeated slip along the deep-seated thrusts, forming the elevated, annular topography within those basins. Finite element modeling by Byrne et al. (2015) also predicted the formation of extensional structures outside the basin rim. Although no basin-circumferential graben have been found at Crisium, Humorum and Serenitatis do show graben surrounding the mascon. This finding further validates the application of this model to the interpretation presented here.

#### 4.2. Factors Controlling the Formation and Expression of Mascon-Bounding Ring Faults

Some expression of an arcuate topographic bench is manifest in all the study basins presented herein but the extent to which this topography is present varies. In the case of both Mare Imbrium (Figure 8a) and Mare Humorum (Figure 6a), basin-circumferential shortening landforms are not typically spatially collocated with an annulus of elevated terrain. These landforms do, however, align with the boundary of the maximum positive Bouguer gravity anomaly values (Figures 6 and 8). Model solutions show that the faults responsible for such landforms in these two basins generally penetrate to depths  $<20$  km and do not fully bound the elevated mantle plug beneath (Table 2, Figures 7 and 9). The absence of mascon-bounding thrust faults at some azimuths suggests that, for these basins at least, only a portion of the uplifted mantle is bounded by an outward-dipping thrust ring-fault system.

The mechanism responsible for this fault architecture (cf., Byrne et al., 2015) likely operated in Imbrium and Humorum. However, other local- or regional-scale factors likely impeded the ability of the faults to propagate fully around the mantle plug or to reach depths of tens of kilometers. It is important to note, too, that this modeling approach only captures deformation that occurred after the maria were emplaced and cooled, thus expressing structural relief. Ghost craters in Maria Crisium and Moscovense, as well as buried craters in Humorum and

Nectaris, imply that some time must have passed between basin formation and mare emplacement. Therefore, it is possible that some of these faults penetrate to greater depths but are rendered inactive after the maria cools.

The thrust fault ring systems we document require a mechanical coupling of the crustal collar surrounding large impact basins with their impact melt sheets in addition (in most cases) to upwelled mantle material (Byrne et al., 2015; Dombard et al., 2013; Freed et al., 2014; Melosh et al., 2013). Since the entirety of a large basin is in a subsostatic state immediately after impact, excavation, and collapse (Dombard et al., 2013; Freed et al., 2014; Melosh et al., 2013), cooling rates must be sufficiently rapid to prevent the mantle from undergoing viscoelastic relaxation and subsidence for such mascon-bounding faults to form. As the subsostatic crustal collar was uplifted, the mechanically coupled melt sheet and the underlying portion of the mantle achieved and maintained a superisostatic state. In the case of Mare Imbrium, locally high abundance of radiogenic KREEP-rich rocks (Lawrence et al., 1998; Wieczorek et al., 2006) might have limited the cooling rate and, in turn, the degree to which this mechanical coupling occurred. Moreover, the sheer size of this basin may have increased the speed at which its melt sheet and any underlying, uplifted mantle attained superisostasy (e.g., Trowbridge et al., 2020).

Mascon formation and preservation are likely affected by a balance between the cooling rates of the impacted material and mantle relaxation rates. Thus, an increased heat flux locally (i.e., at the impact site) or even globally at the time of impact (for, say, an earlier point in lunar history) might have sufficiently decreased the Maxwell time of the uplifted mantle to allow for a sufficiently rapid relaxation such that a thrust ring fault could only partially form. It is likely, then, that some combination of the location, size, and timing of a given basin-forming impact event contributes to the nature and behavior of postimpact modification. For Imbrium and Humorum, as well as the northwestern boundary of the Nectaris basin, the proximity to Oceanus Procellarum (Figure 1)—the region with the highest heat flux (Wieczorek et al., 2006) and most recent mare volcanism (Hiesinger et al., 2000, 2011)—could have impeded the formation of these structures.

Another factor that may affect the development of deep-seated thrusts is the size of the basin in question. Basin size may be particularly important in the case of Mare Imbrium, where the basin subtends about  $36^{\circ}$  of arc, or about 10% of the lunar circumference, in contrast to Mare Nectaris, which subtends about  $10^{\circ}$  of arc and has a well-expressed (partial) ring-fault system. The size of Imbrium, and therefore the curvature of the basin floor, increases the magnitude of membrane stresses at the basin. For a given crustal thickness, increased membrane stresses at Imbrium can likely support elastically a greater topographic load than can smaller basins, thus limiting the degree to which circumferential thrust faults can develop. The curvature of the lunar surface was not considered in either our models or the study by Byrne et al. (2015) but is important in fully considering the entire stress state associated with basin loading (e.g., Freed et al., 2001); future studies should explore the effects of curvature in testing our findings for the specific basins we discuss here.

Where faults do not penetrate to depths of tens of kilometers but do extend below the base of the mare infill, some local mechanical or stratigraphic impediment may hinder or arrest further downward propagation (cf., Cooke & Underwood, 2001; Gross et al., 1997; Nicol et al., 1996; Schultz et al., 2006). This outcome might be the case in Mare Humorum, where relatively shallow, listric faults shoal into a subhorizontal detachment at depths of  $<10$  km (Figure 7). This detachment could represent the upper boundary of a more competent rock layer with lower fracture density or some thermal or rheological discontinuity at the time of their formation. It is plausible, too, that multiple mechanisms (e.g., cooling and subsidence of the mare basalts) can be invoked to explain the formation of wrinkle ridges within these basins. Estimates of present lunar lithospheric thickness are variable but typically suggest an elastic thickness of  $<100$  km (Comer et al., 1979; Crosby & McKenzie, 2005; Kuckes, 1977; Solomon & Head, 1980; Williams et al., 1995). The thick, elastic lithosphere should allow for continued downward fault propagation, assuming that tectonic forcing is sufficient to match the confining stress and yield strength of the lower lithosphere and induce slip. However, under the assumption that the effective elastic thickness early in the Moon's history was inversely proportional to heat flux, and that isostatic adjustment has mostly ended, then the maximum penetration depth of these faults would be correspondingly less than is possible today.

Indeed, the finding that faults within these lunar mare basins generally penetrate to depths of less than 30 km can, in part, be explained by an elastic lithosphere that was meaningfully less thick when these basins formed than it is today. It is also likely that, as the Moon progressively cooled, the lunar mantle's ability to deform viscoelastically was impeded and thus the elevated superisostatic mantle plug and the coupled subsostatic crustal collar became immobilized. Impairment of the basin's ability to adjust isostatically would thus limit the ability of faults to continue to propagate, especially as the differential stress required for slip would increase proportionally with

depth. Presumably, then, at some point the magnitude of the differential stress was insufficient to overcome the strength of the mechanical lithosphere at depths greater than about 30 km.

#### 4.3. Deep-Seated Thrust Faults on the Moon and Beyond

Our results from this study demonstrate that the faults responsible for producing circumferential landforms within several of the lunar mare basins penetrate to greater depths than the base of the volcanic infill (Williams & Zuber, 1998) (Table 2); the average penetration depth of faults detailed in this study is  $22 \pm 3$  km. Downward fault propagation and brittle deformation, therefore, continues into the lower lunar crust and, in some cases, the upper mantle (Table 2).

Not only do outward-dipping thrust faults typically penetrate to a considerable depth, well beyond the base of the thickest mare deposits, they are generally subparallel to the crust–mantle interface beneath the study basins. Our findings thus indicate that the mechanical coupling of a subisostatic crustal collar and superisostatic mantle plug, and the resulting partial or near-encircling thrust ring-fault system, is characteristic of large impact basins on the Moon in general (where “large” is greater than or equal to our smallest case study basin, Mare Nectaris, of  $D = 340$  km).

Despite the ubiquitous nature of mascons within the lunar mare basins, the preservation of these gravity signatures on other terrestrial planets remains unclear. Large impact basins subsequently deformed by tectonic activity are evident on Mars (e.g., Hellas, Argyre, Isidis, and Utopia) and Mercury (e.g., Caloris and Rembrandt). However, of the largest Martian impact basins, Isidis is the only instance characterized by a mascon such as that observed on the Moon (Arkani-Hamed, 2009; Yuan et al., 2001), although we note that Argyre does have a positive free-air gravity anomaly signature. Ancient, elevated heat flow inducing viscous deformation of the lower crust on Mars may have inhibited mascon formation (Karimi et al., 2016; Mohit & Phillips, 2007). The relative absence of such mascons on Mars supports this view, as does the lack of basin-circumferential shortening landforms such as those detailed here for mascon basins on the Moon.

In the case of Mercury, Caloris (Smith et al., 2012) and Subkou (Phillips et al., 2018) are the only large impact basins with a confirmed positive free-air gravity anomaly. Curiously, many basins on Mercury have a scarp on the basin rim that verges outward, opposite of what is seen for the Moon (Fegan et al., 2017). The nature of the positive gravity signature for Caloris is currently unknown and may be the product of elevated topography within the basin (Dombard et al., 2013; Smith et al., 2012). However, the apparent lack of mascon basins on Mercury might simply reflect the relatively low-resolution and globally incomplete gravity field data available from the MErcury Surface, Space ENvironment, GEochemistry, and Ranging (MESSENGER) spacecraft, which had an orbital periapsis situated in the mid-northern hemisphere (Genova et al., 2019). Thus, further investigation of the Mercury gravity field by BepiColombo upon its expected arrival in 2025 (Imperi et al., 2018) may provide further insight into basin formation and properties on the innermost planet.

Nonetheless, the apparent relative scarcity of mascon-bearing impact basins on Mars and Mercury suggests that this phenomenon is not ubiquitous across the inner Solar System. The few mascon basins on Mars and Mercury lack a basin-circumferential topographic bench, as seen in the lunar basins presented herein. If some characteristic(s) of lunar thermal evolution or impact history encourages the formation of mascon-bounding, deep-seated thrust faults as the geometric consequence of mantle subsidence coupled with the uplift of a crustal collar, then this process might indeed be unique to the Moon. This particular fault architecture could be the result of a specific combination of cooling rates, the thermal state of the lower lunar lithosphere, the rheological properties of the lunar crust, and the longevity of mantle subsidence coupled with crustal uplift.

### 5. Conclusion

Several mascon-bearing basins on the Moon—those hosting Maria Imbrium, Serenitatis, Humorum, Nectaris, and Mosoviense—boast portions of arcuate, elevated topography within their perimeters that reflect reverse slip along relatively deep-seated ( $22 \pm 3$  km), low-angle ( $25^\circ \pm 2^\circ$ ) thrust faults. In most cases, these structures geometrically bound the elevated mantle plug beneath each basin; this architecture is evident for both near- and far-side basins. The expression of this geometric arrangement, however, is not uniform for all study basins. The processes responsible for these structures within Serenitatis, Nectaris, and Mosoviense likely share a genesis

with those structures documented for Mare Crisium (Byrne et al., 2015), but the growth of mascon-bounding thrust ring faults has been inhibited, to some degree, for Imbrium and Humorum. Mascon basins appear rare on Mercury and Mars, and no such basin on either world shows as well defined a set of arcuate, elevated topography as the lunar features studied here. Whether the reported structural architecture for the lunar basins we consider here is a representative of large mascon-bearing basins on rocky planets in general remains unclear.

## Data Availability Statement

All data are available at Collins (2021a). The SLDEM2015 digital elevation model (Barker et al., 2016) was obtained from the NASA Planetary Data System and is available at <https://pgda.gsfc.nasa.gov/products/54>. The degree-and-order 660 Bouguer gravity anomaly map (Zuber et al., 2013) from the Gravity Recovery and Interior Laboratory (GRAIL) is available at <https://pgda.gsfc.nasa.gov/products/50>. The GRAIL-derived crustal thickness model from Wieczorek et al. (2013) is available at Wieczorek (2012). The codes used to conduct this analysis are available at Collins (2021b).

## Acknowledgments

This work was supported by the NASA Lunar Data Analysis Program (LDAP) Grant 80NSSC17K0411. This research made use of NASA's Planetary Data System and Astrophysics Data System.

## References

- Acocella, V. (2006). Caldera types: How end-members relate to evolutionary stages of collapse. *Geophysical Research Letters*, 33(18), L18314. <https://doi.org/10.1029/2006gl027434>
- Acocella, V. (2007). Understanding caldera structure and development: An overview of analogue models compared to natural calderas. *Earth-Science Reviews*, 85(3–4), 125–160. <https://doi.org/10.1016/j.earscirev.2007.08.004>
- Andrews-Hanna, J. C., Head, J. W., Johnson, B. C., Keane, J. T., Kiefer, W. S., McGovern, P. J., et al. (2018). Ring faults and ring dikes around the Orientale basin on the Moon. *Icarus*, 310, 1–20. <https://doi.org/10.1016/j.icarus.2017.12.012>
- Arkani-Hamed, J. (2009). Polar wander of Mars: Evidence from giant impact basins. *Icarus*, 204(2), 489–498. <https://doi.org/10.1016/j.icarus.2009.07.020>
- Barker, M. K., Mazarico, E., Neumann, G. A., Zuber, M. T., Haruyama, J., & Smith, D. E. (2016). A new lunar digital elevation model from the Lunar Orbiter Laser Altimeter and SELENE Terrain Camera. *Icarus*, 273, 346–355. <https://doi.org/10.1016/j.icarus.2015.07.039>
- Bryan, W. B. (1973). Wrinkle-ridges as deformed surface crust on ponded mare lava. In *Lunar and Planetary Science Conference Proceedings* (Vol. 4, p. 93).
- Burchardt, S., & Walter, T. R. (2010). Propagation, linkage, and interaction of caldera ring-faults: Comparison between analogue experiments and caldera collapse at Miyakejima, Japan, in 2000. *Bulletin of Volcanology*, 72(3), 297–308. <https://doi.org/10.1007/s00445-009-0321-7>
- Byrne, P. K., Klimczak, C., McGovern, P. J., Mazarico, E., James, P. B., Neumann, G. A., et al. (2015). Deep-seated thrust faults bound the Mare Crisium lunar mascon. *Earth and Planetary Science Letters*, 427, 183–190. <https://doi.org/10.1016/j.epsl.2015.06.022>
- Collins, M. (2021a). Searching for deep-seated thrust faults on the moon (version 4) [Dataset]. Dryad. Retrieved from <http://esgf-node.llnl.gov/projects/cmip6>
- Collins, M. (2021b). Searching for deep-seated thrust faults on the moon. *Zenodo*. <https://doi.org/10.5281/ZENODO.5055815>
- Comer, R. P., Solomon, S. C., & Head, J. W. (1979). Elastic lithosphere thickness on the moon from mare tectonic features – A formal inversion. In *Lunar and Planetary Science Conference Proceedings* (Vol. 10, pp. 2441–2463).
- Cooke, M. L., & Underwood, C. A. (2001). Fracture termination and step-over at bedding interfaces due to frictional slip and interface opening. *Journal of Structural Geology*, 23(2–3), 223–238. [https://doi.org/10.1016/s0191-8141\(00\)00092-4](https://doi.org/10.1016/s0191-8141(00)00092-4)
- Crosby, A., & McKenzie, D. (2005). Measurements of the elastic thickness under ancient lunar terrain. *Icarus*, 173(1), 100–107. <https://doi.org/10.1016/j.icarus.2004.07.017>
- Dombard, A. J., Hauck, S. A., & Balcerski, J. A. (2013). On the origin of mascon basins on the Moon (and beyond). *Geophysical Research Letters*, 40(1), 28–32. <https://doi.org/10.1029/2012GL054310>
- Fassett, C. I., Head, J. W., Kadish, S. J., Mazarico, E., Neumann, G. A., Smith, D. E., & Zuber, M. T. (2012). Lunar impact basins: Stratigraphy, sequence and ages from superposed impact crater populations measured from Lunar Orbiter Laser Altimeter (LOLA) data. *Journal of Geophysical Research*, 117(E12), E00H06. <https://doi.org/10.1029/2011je003951>
- Fegan, E. R., Rothery, D. A., Marchi, S., Massironi, M., Conway, S. J., & Anand, M. (2017). Late movement of basin-edge lobate scarps on Mercury. *Icarus*, 288, 226–234. <https://doi.org/10.1016/j.icarus.2017.01.005>
- Freed, A. M., Johnson, B. C., Blair, D. M., Melosh, H. J., Neumann, G. A., Phillips, R. J., et al. (2014). The formation of lunar mascon basins from impact to contemporary form. *Journal of Geophysical Research: Planets*, 119(11), 2378–2397. <https://doi.org/10.1002/2014je004657>
- Freed, A. M., Melosh, H. J., & Solomon, S. C. (2001). Tectonics of mascon loading: Resolution of the strike-slip faulting paradox. *Journal of Geophysical Research*, 106(E9), 20603–20620. <https://doi.org/10.1029/2000je001347>
- Genova, A., Goossens, S., Mazarico, E., Lemire, F. G., Neumann, G. A., Kuang, W., et al. (2019). Geodetic evidence that Mercury has a solid inner core. *Geophysical Research Letters*, 46(7), 3625–3633. <https://doi.org/10.1029/2018gl081135>
- Geyer, A., & Martí, J. (2014). A short review of our current understanding of the development of ring faults during collapse caldera formation. *Frontiers of Earth Science*, 2, 22. <https://doi.org/10.3389/feart.2014.00022>
- Gillis, J. J., & Spudis, P. D. (2000). Geology of the Smythii and Marginis region of the Moon: Using integrated remotely sensed data. *Journal of Geophysical Research*, 105(E2), 4217–4233. <https://doi.org/10.1029/1999je001111>
- Golombok, M. P. (1985). Fault type predictions from stress distributions on planetary surfaces: Importance of fault initiation depth. *Journal of Geophysical Research*, 90(B4), 3065–3074. <https://doi.org/10.1029/jb090ib04p03065>
- Golombok, M. P., Anderson, F. S., & Zuber, M. T. (2001). Martian wrinkle ridge topography: Evidence for subsurface faults from MOLA. *Journal of Geophysical Research*, 106(E10), 23811–23821. <https://doi.org/10.1029/2000je001308>
- Golombok, M. P., Plescia, J. B., & Franklin, B. J. (1991). Faulting and folding in the formation of planetary wrinkle ridges. *Lunar and Planetary Science Conference Proceedings*, 21, 679–693.
- Gross, M. R., Gutie, G., Bai, T., Wacker, M. A., Collinsworth, K. B., & Behl, R. J. (1997). Influence of mechanical stratigraphy and kinematics on fault scaling relations. *Journal of Structural Geology*, 19(2), 171–183. [https://doi.org/10.1016/s0191-8141\(96\)00085-5](https://doi.org/10.1016/s0191-8141(96)00085-5)

- Hiesinger, H., Head, J. W., Wolf, U., Jaumann, R., & Neukum, G. (2011). Ages and stratigraphy of lunar mare basalts: A synthesis. *Recent Advances and Current Research Issues in Lunar Stratigraphy*, 477, 1–51.
- Hiesinger, H., Head, J. W., III, Wolf, U., Jaumann, R., & Neukum, G. (2010). Ages and stratigraphy of lunar mare basalts in Mare Frigoris and other near side maria based on crater size-frequency distribution measurements. *Journal of Geophysical Research*, 115(E3), E03003. <https://doi.org/10.1029/2009je003380>
- Hiesinger, H., Jaumann, R., Neukum, G., & Head, J. W., III. (2000). Ages of mare basalts on the lunar near side. *Journal of Geophysical Research*, 105(E12), 29239–29275. <https://doi.org/10.1029/2000je001244>
- Imperi, L., less, L., & Mariani, M. J. (2018). An analysis of the geodesy and relativity experiments of BepiColombo. *Icarus*, 301, 9–25. <https://doi.org/10.1016/j.icarus.2017.09.008>
- Ishihara, Y., Morota, T., Nakamura, R., Goossens, S., & Sasaki, S. (2011). Anomalous Moscoviene basin: Single oblique impact or double impact origin? *Geophysical Research Letters*, 38(3), L03201. <https://doi.org/10.1029/2010gl045887>
- Johnson, B. C., Blair, D. M., Collins, G. S., Melosh, H. J., Freed, A. M., Taylor, G. J., et al. (2016). Formation of the Orientale lunar multiring basin. *Science*, 354(6311), 441–444. <https://doi.org/10.1126/science.aag0518>
- Karimi, S., Dombard, A. J., Buczkowski, D. L., Robbins, S. J., & Williams, R. M. (2016). Using the viscoelastic relaxation of large impact craters to study the thermal history of Mars. *Icarus*, 272, 102–113. <https://doi.org/10.1016/j.icarus.2016.02.037>
- Kuckes, A. F. (1977). Strength and rigidity of the elastic lunar lithosphere and implications for present-day mantle convection in the Moon. *Physics of the Earth and Planetary Interiors*, 14(1), 1–12. [https://doi.org/10.1016/0031-9201\(77\)90042-5](https://doi.org/10.1016/0031-9201(77)90042-5)
- Lawrence, D. J., Feldman, W. C., Barracough, B. L., Binder, A. B., Elphic, R. C., Maurice, S., & Thomsen, D. R. (1998). Global elemental maps of the Moon: The Lunar Prospector gamma-ray spectrometer. *Science*, 281(5382), 1484–1489. <https://doi.org/10.1126/science.281.5382.1484>
- Levy, S., Bohnenstiehl, D. R., Sprinkle, P., Boettcher, M. S., Wilcock, W. S. D., Tolstoy, M., & Waldhauser, F. (2018). Mechanics of fault reactivation before, during, and after the 2015 eruption of Axial Seamount. *Geology*, 46(5), 447–450. <https://doi.org/10.1130/g39978.1>
- Lin, J., & Stein, R. S. (2004). Stress triggering in thrust and subduction earthquakes and stress interaction between the southern San Andreas and nearby thrust and strike-slip faults. *Journal of Geophysical Research*, 109(B2), B02303. <https://doi.org/10.1029/2003jb002607>
- Mangold, N., Allemand, P., & Thomas, P. G. (1998). Wrinkle ridges of Mars: Structural analysis and evidence for shallow deformation controlled by ice-rich décollements. *Planetary and Space Science*, 46(4), 345–356. [https://doi.org/10.1016/0032-0633\(97\)00195-5](https://doi.org/10.1016/0032-0633(97)00195-5)
- Maurer, P., Eberhardt, P., Geiss, J., Grögler, N., Stettler, A., Brown, G. M., et al. (1978). Pre-Imbrian craters and basins: Ages, compositions and excavation depths of Apollo 16 breccias. *Geochimica et Cosmochimica Acta*, 42(11), 1687–1720. [https://doi.org/10.1016/0016-7037\(78\)90257-0](https://doi.org/10.1016/0016-7037(78)90257-0)
- Maxwell, T. A., El-Baz, F., & Ward, S. H. (1975). Distribution, morphology, and origin of ridges and arches in Mare Serenitatis. *The Geological Society of America Bulletin*, 86(9), 1273–1278. [https://doi.org/10.1130/0016-7606\(1975\)86<1273:dmaoor>2.0.co;2](https://doi.org/10.1130/0016-7606(1975)86<1273:dmaoor>2.0.co;2)
- Melosh, H. J. (1978). The tectonics of mascon loading. *Lunar and Planetary Science Conference Proceedings*, 9, 3513–3525.
- Melosh, H. J., Freed, A. M., Johnson, B. C., Blair, D. M., Andrews-Hanna, J. C., Neumann, G. A., et al. (2013). The origin of lunar mascon basins. *Science*, 340(6140), 1552–1555. <https://doi.org/10.1126/science.1235768>
- Miljković, K., Wieczorek, M. A., Collins, G. S., Laneuville, M., Neumann, G. A., Melosh, H. J., et al. (2013). Asymmetric distribution of lunar impact basins caused by variations in target properties. *Science*, 342(6159), 724–726. <https://doi.org/10.1126/science.1243224>
- Mohit, P. S., & Phillips, R. J. (2007). Viscous relaxation on early Mars: A study of ancient impact basins. *Geophysical Research Letters*, 34(21), L21204. <https://doi.org/10.1029/2007gl031252>
- Montési, L. G., & Zuber, M. T. (2003). Clues to the lithospheric structure of Mars from wrinkle ridge sets and localization instability. *Journal of Geophysical Research*, 108(E6), 5048. <https://doi.org/10.1029/2002je001974>
- Muller, P. M., & Sjogren, W. L. (1968). Mascons: Lunar mass concentrations. *Science*, 161(3842), 680–684. <https://doi.org/10.1126/science.161.3842.680>
- Nahm, A. L., Oehman, T., & Kring, D. A. (2013). Normal faulting origin for the Cordillera and Outer Rook rings of Orientale Basin, the Moon. *Journal of Geophysical Research: Planets*, 118(2), 190–205. <https://doi.org/10.1002/jgre.20045>
- Neukum, G., & Ivanov, B. A. (1994). Crater size distributions and impact probabilities on Earth from lunar, terrestrial-planet, and asteroid cratering data. *Hazards due to Comets and Asteroids*, 1, 359–416. <https://doi.org/10.2307/j.ctv23khmpv.18>
- Neumann, G. A., Zuber, M. T., Smith, D. E., & Lemoine, F. G. (1996). The lunar crust: Global structure and signature of major basins. *Journal of Geophysical Research*, 101(E7), 16841–16863. <https://doi.org/10.1029/96je01246>
- Nicol, A., Watterson, J., Walsh, J. J., & Childs, C. (1996). The shapes, major axis orientations and displacement patterns of fault surfaces. *Journal of Structural Geology*, 18(2–3), 235–248. [https://doi.org/10.1016/s0191-8141\(96\)80047-2](https://doi.org/10.1016/s0191-8141(96)80047-2)
- Okada, Y. (1992). Internal deformation due to shear and tensile faults in a half-space. *Bulletin of the Seismological Society of America*, 82(2), 1018–1040. <https://doi.org/10.1785/bssa0820021018>
- Phillips, R. J., Byrne, P. K., James, P. B., Mazarico, E., Neumann, G. A., & Perry, M. E. (2018). Mercury's crust and lithosphere: Structure and mechanics. *Mercury: The view after MESSENGER*, 52–84.
- Potter, R. W. (2015). Investigating the onset of multi-ring impact basin formation. *Icarus*, 261, 91–99. <https://doi.org/10.1016/j.icarus.2015.08.009>
- Potter, R. W., Kring, D. A., Collins, G. S., Kiefer, W. S., & McGovern, P. J. (2013). Numerical modeling of the formation and structure of the Orientale impact basin. *Journal of Geophysical Research: Planets*, 118(5), 963–979. <https://doi.org/10.1002/jgre.20080>
- Schultz, R. A. (2000). Localization of bedding plane slip and backthrust faults above blind thrust faults: Keys to wrinkle ridge structure. *Journal of Geophysical Research*, 105(E5), 12035–12052. <https://doi.org/10.1029/1999je001212>
- Schultz, R. A., Okubo, C. H., & Wilkins, S. J. (2006). Displacement-length scaling relations for faults on the terrestrial planets. *Journal of Structural Geology*, 28(12), 2182–2193. <https://doi.org/10.1016/j.jsg.2006.03.034>
- Smith, D. E., Zuber, M. T., Phillips, R. J., Solomon, S. C., Hauck, S. A., Lemoine, F. G., et al. (2012). Gravity field and internal structure of Mercury from MESSENGER. *Science*, 336(6078), 214–217. <https://doi.org/10.1126/science.1218809>
- Solomon, S. C., & Head, J. W. (1980). Lunar mascon basins: Lava filling, tectonics, and evolution of the lithosphere. *Reviews of Geophysics*, 18(1), 107–141. <https://doi.org/10.1029/rg018i001p00107>
- Speyerer, E. J., Robinson, M. S., & Denevi, B. W., & LROC Science Team. (2011). Lunar Reconnaissance Orbiter Camera global morphological map of the Moon. *Lunar and Planetary Science Conference*, 42, 2387.
- Stöffler, D., & Ryder, G. (2001). Stratigraphy and isotope ages of lunar geologic units: Chronological standard for the inner solar system. In *Chronology and evolution of Mars* (pp. 9–54).
- Stöffler, D., Ryder, G., Ivanov, B. A., Artemieva, N. A., Cintala, M. J., & Grieve, R. A. (2006). Cratering history and lunar chronology. *Reviews in Mineralogy and Geochemistry*, 60(1), 519–596. <https://doi.org/10.2138/rmg.2006.60.05>
- Toda, S., Stein, R. S., Richards-Dinger, K., & Bozkurt, S. B. (2005). Forecasting the evolution of seismicity in southern California: Animations built on earthquake stress transfer. *Journal of Geophysical Research*, 110(B5), B05S16. <https://doi.org/10.1029/2004jb003415>

- Trowbridge, A. J., Johnson, B. C., Freed, A. M., & Melosh, H. J. (2020). Why the lunar South Pole–Aitken Basin is not a mascon. *Icarus*, 352, 113995. <https://doi.org/10.1016/j.icarus.2020.113995>
- Vaughan, W. M., Head, J. W., Wilson, L., & Hess, P. C. (2013). Geology and petrology of enormous volumes of impact melt on the Moon: A case study of the Orientale basin impact melt sea. *Icarus*, 223(2), 749–765. <https://doi.org/10.1016/j.icarus.2013.01.017>
- Watters, T. R. (1991). Origin of periodically spaced wrinkle ridges on the Tharsis Plateau of Mars. *Journal of Geophysical Research*, 96(E1), 15599–15616. <https://doi.org/10.1029/91je01402>
- Wedepohl, K. H. (1981). Tholeiitic basalts from spreading ocean ridges the growth of the oceanic crust. *Naturwissenschaften*, 68(3), 110–119. <https://doi.org/10.1007/bf01047247>
- Wieczorek, M. A. (2012). Grail crustal thickness archive [Dataset]. Zenodo. <https://doi.org/10.5281/ZENODO.997347>
- Wieczorek, M. A., Jolliff, B. L., Khan, A., Pritchard, M. E., Weiss, B. P., Williams, J. G., et al. (2006). The constitution and structure of the lunar interior. *Reviews in Mineralogy and Geochemistry*, 60(1), 221–364. <https://doi.org/10.2138/rmg.2006.60.3>
- Wieczorek, M. A., Neumann, G. A., Nimmo, F., Kiefer, W. S., Taylor, G. J., Melosh, H. J., et al. (2013). The crust of the Moon as seen by GRAIL. *Science*, 339(6120), 671–675. <https://doi.org/10.1126/science.1231530>
- Wieczorek, M. A., & Phillips, R. J. (2000). The “Procellarum KREEP Terrane”: Implications for mare volcanism and lunar evolution. *Journal of Geophysical Research*, 105(E8), 20417–20430. <https://doi.org/10.1029/1999je001092>
- Williams, K. K., Neumann, G. A., & Zuber, M. T. (1995). Lunar mascon basins: Analysis of effective elastic lithosphere thickness using gravity anomaly models. In *Lunar and Planetary Science Conference* (Vol. 26).
- Williams, K. K., & Zuber, M. T. (1998). Measurement and analysis of lunar basin depths from Clementine altimetry. *Icarus*, 131(1), 107–122. <https://doi.org/10.1006/icar.1997.5856>
- Wilson, L., & Head, J. W. (2011). Impact melt sheets in lunar basins: Estimating thickness from cooling behavior. *Lunar and Planetary Science Conference*, 42, 1345.
- Yingst, R. A., & Head, J. W., III. (1997). Volumes of lunar lava ponds in South Pole-Aitken and Orientale basins: Implications for eruption conditions, transport mechanisms, and magma source regions. *Journal of Geophysical Research*, 102(E5), 10909–10931. <https://doi.org/10.1029/97je00717>
- Yingst, R. A., & Head, J. W., III. (1998). Characteristics of lunar mare deposits in Smythii and Marginis basins: Implications for magma transport mechanisms. *Journal of Geophysical Research*, 103(E5), 11135–11158. <https://doi.org/10.1029/98je00736>
- Yingst, R. A., & Head, J. W., III. (1999). Geology of mare deposits in South Pole-Aitken basin as seen by Clementine UV/VIS data. *Journal of Geophysical Research*, 104(E8), 18957–18979. <https://doi.org/10.1029/1999je900016>
- Yuan, D. N., Sjogren, W. L., Konopliv, A. S., & Kucinskas, A. B. (2001). Gravity field of Mars: A 75th degree and order model. *Journal of Geophysical Research*, 106(E10), 23377–23401. <https://doi.org/10.1029/2000je001302>
- Zisk, S., Adams, J., Head, J. W., McCord, T. B., & Pieters, C. (1978). Topographic evolution of Mare Crisium and its relation to mare filling. In *Lunar and Planetary Science Conference* (Vol. 9, pp. 1297–1299).
- Zuber, M. T. (1995). Wrinkle ridges, reverse faulting, and the depth penetration of lithospheric stress in Lunae Planum Mars. *Icarus*, 114(1), 80–92. <https://doi.org/10.1006/icar.1995.1045>
- Zuber, M. T., Smith, D. E., Neumann, G. A., Goossens, S., Andrews-Hanna, J. C., Head, J. W., et al. (2016). Gravity field of the Orientale basin from the Gravity Recovery and Interior Laboratory Mission. *Science*, 354(6311), 438–441. <https://doi.org/10.1126/science.aag0519>
- Zuber, M. T., Smith, D. E., Watkins, M. M., Asmar, S. W., Konopliv, A. S., Lemoine, F. G., et al. (2013). Gravity field of the Moon from the Gravity Recovery and Interior Laboratory (GRAIL) Mission. *Science*, 339(6120), 668–671. <https://doi.org/10.1126/science.1231507>